NUREG/CR-1444

Investigation of Distorted-Geometry Simulation of Pool Dynamics in Horizontal-Vent BWR Containments

Prepared by N.G. Ruggieri, A.A. Sonin

Department of Mechanical Engineering
Massachusetts Institute of Technology

Prepared for
U.S. Nuclear Regulatory Commission

Available from

GPO Sales Program
Division of Technical Information and Document Control
U. S. Nuclear Regulatory Commission
Washington, D. C. 20555

and

National Technical Information Service
Springfield, Virginia 22161

NUREG/CR-1444
R4

Investigation of Distorted-Geometry Simulation of Pool Dynamics in Horizontal-Vent BWR Containments

Manuscript Completed: May 1979
Date Published: April 1980

Prepared by
N.G. Ruggieri, A.A. Sonin

Department of Mechanical Engineering
Massachusetts Institute of Technology
Cambridge, MA 02139

Prepared for
Division of Reactor Safety Research
Office of Nuclear Regulatory Research
U. S. Nuclear Regulatory Commission
Washington, D.C. 20555
NRC FIN No. B6167

ABSTRACT

Experiments were conducted to investigate the accuracy of distorted-geometry testing of pool dynamics in horizontal-vent BWR containments. Distorted-geometry testing implies testing in systems where the flow-wise dimensions are full scale, but all dimensions transverse to the flow are reduced in the same proportion. The assumption is that flow velocities, pressures and other thermodynamic properties can be interpreted as being the same in the distorted-geometry system as in its correctly proportioned counterpart. Our experiments, which were done at small scale using the established scaling laws, showed that the geometric distortions can have a significant effect on the pool swell under conditions which are roughly representative of horizontal-vent BWR containment systems during a LOCA. Breakthrough occurred later, the water ligament was thicker, and pool velocity lower in a system where the cross-sectional areas were reduced by a factor of three. Some reasons for the differences are discussed.

TABLE OF CONTENTS

LIST OF FIGURES

LIST OF FIGURES (cont')

SYMBOLS

A_p	cross-sectional area of vertical feed pipe
A_v	cross-sectional area of horizontal vent
b	system breadth (long dimension)
C_m	mass flux coefficient, Eq.(3) of Ref. 7.
d	diameter of horizontal vent
g	acceleration of gravity, 9.80 ms^{-2}
h	system height
k	vent system frictional loss coefficient for water clearing
ℓ_v	length of horizontal vent
p	absolute pressure
p_w	absolute pressure in wetwell airspace
p_D	absolute pressure in drywell
Δp	amplitude of pool pressure oscillations due to wall oscillations (App. A)
R	specific gas constant for drywell gas
s	submergence of horizontal vent (centerline)
t	time
t_o	vent clearing time
t*	time when air reaches upstream end of horizontal vent (App. B)
T_D	drywell gas temperature
V	instantaneous upward velocity of pool (App. B)
V_o	see Eq. (B.8), App. B
V_p	instantaneous downward velocity of water in vertical feed pipe
V_v	instantaneous water velocity in vent
w	system width (short dimension)

x in Figs. 32 and 33, horizontal displacement from vent exit; in Appendix A, see Fig. A.1; in Appendix B, see Fig. B.1

x' in Appendix B, see Fig. B.1

x_o in Appendix A, amplitude of wall displacement (see Fig. A.1)

y see Fig. A.1

z see Fig. A.1

z_a value of z at point where acceleration is measured (Appendix A).

z_w value of z at free water surface in pool (Appendix A).

γ specific heat ratio c_p/c_v

π_1 to π_4 see Eqs. (1) - (4)

ρ water density

τ window oscillation period in Appendix A; vent flow characteristic time, given by Eq. (B.9), in Appendix B.

1. INTRODUCTION

Two approaches have been used to develop design loads for BWR pressure suppression containments under postulated accident conditions from out-of-scale experiments. One approach relies on small scale modeling of the processes, and is based on a knowledge of the scaling laws which ensure dynamic similarity between the model and the full scale system. This method has been used to predict the air clearing loads for the General Electric Corporation's Mark I and Mark II BWR containments [1-5]. The scaling laws have been verified experimentally [6-9].

The other approach relies on tests in distorted-geometry systems where the flow-wise (usually vertical) dimensions of the test system are full scale, but all dimensions transverse to the flow are reduced in the same proportion. Full scale driving pressures and flow rates per unit area are imposed, and measured pressures and velocities are assumed to be equal to those in the full scale prototype system. In other words, the method assumes that the flow is essentially independent of its extent transverse to the flow direction. The GE Mark III containment design has relied heavily on this kind of simulation [10].

Distorted-geometry tests are used where completely full-scale tests would require prohibitively high flow rates, even for a representative single "cell" of a large system. In principle, they have the advantage over small scale simulations that no à priori knowledge is needed of the

scaling laws: quantities are simply assumed to be equal to the full scale values. The shortcoming of distorted-geometry tests lies in the fact that little information is available on when they can be expected to yield accurate results.

This paper describes a study of the accuracy of distorted-geometry testing in a situation which is characteristic of the pool swell process in a horizontal-vent BWR pressure-suppression containment. Our premise is that the scaling laws for this process have already been established [6-9], and that a check of the distorted-geometry testing concept can therefore be carried out at a small scale.

Our study was conducted in small-scale systems which were roughly similar to the GE Mark III containment and its distorted-geometry counterpart. Test conditions were chosen to simulate Mark III dynamic conditions approximately. No attempt was made, however, to simulate any particular system or event exactly. The purpose of our investigation was to check the accuracy of distorted-geometry testing under conditions which were typical of applications.

2. EXPERIMENTS

Comparison tests were performed in three small-scale systems shown in Figs. 1 and 2. Tables 1 and 2 summarize the geometrical and dynamical conditions, respectively, in the tests. The systems simulated a simple wet pressure suppression containment system with a single horizontal

vent. The pool had a rectangular cross-section, and the vent and its vertical feed pipe were of circular cross-section. All three systems had the same flow-wise dimension* (vent length, distance from floor to vent, and submergence, the latter being adjustable). The dimensions transverse to the flow (system width, system breadth, vent diameter, vertical pipe diameter) were in constant proportion to each other in each system, but the absolute values differed in the three systems. System A had proportions roughly similar to the GE Mark III system, except that it had a single vent rather than three. System B had cross-sectional areas 1/3 of those in system A and was therefore a "1/3-scale" distorted-geometry representation of system A. System C had cross-sectional areas 1/9 of those in system A.

A vertical feed pipe linked the horizontal vent to a "drywell" via a calibrated flow-adjustment orifice and fast-opening, pneumatically operated valve similar to the one in [7]. In any particular set of comparison tests, the "wetwell" pressure above the pool was set at a value p_W and the drywell pressure was set at a higher value p_D (Table 2). The initial pressure of the gas trapped below the valve was the same as the wetwell pressure in all runs. A transient was initiated by opening the valve. The valve opening time was short and did not affect the ensuing

*Actually the distance from the vent centerline down to the bottom of the vertical pipe differed in the three systems, being 14, 10 and 9 cm in systems A, B and C respectively. Since this part of the pipe remains filled with stagnant water, it should have no effect on the flow.

flow process significantly. During the entire recorded transient, both P_D and P_W remained essentially fixed at their initial values because the drywell had a large volume and the wetwells of the three systems were connected to an auxiliary tank which also had a large volume (Fig. 2). The calibrated orifice was used to adjust the gas blowdown rate according to the required scaling laws [1-9] and to ensure that the gas flow rate per unit flow area was the same in all three systems in a given comparison test.

The rectangular wetwells of systems B and C were constructed of 1 1/2 in (3.8 cm) thick plexiglas on all sides, while in system A the large side walls were made of 3/4 in (1.9 cm) thick tempered glass, with the remaining sides of 1 1/2 in plexiglas as in the smaller systems. The vents and the vertical pipes were made of plexiglas tubing.

The test sections were fitted with pressure taps (for Kistler Model 205 low-pressure piezotron transducers) at five locations, numbers 1 to 5 on Fig. 2. Transducer responses were recorded on an oscilloscope.

High-speed films (1000 frames per second) were taken of the pool swell from the broad side of the systems.

In all tests the working gas was air, and the liquid water, both at room temperature. Except where indicated, the water was doped with surfactant to minimize the presence of air bubbles on the walls [7, 9].

The dynamic conditions of the tests were chosen so that they would be roughly representative of a loss-of coolant accident in a full-scale

system of comparable geometry. Dynamic conditions are modeled by four dimensionless parameters [8]:

$$\pi_1 = \gamma \tag{1}$$

$$\pi_2 = p_w/\rho g \ell_v \tag{2}$$

$$\pi_3 = p_D/p_w \tag{3}$$

$$\pi_4 = c_m \, (RT_D/g\ell_v)^{1/2} \tag{4}$$

where ℓ_v is the horizontal vent length, taken here as the characteristic length of the systems, ρ is the water density, g is the gravitational acceleration, R is the specific gas constant for air, T_D is the drywell air temperature, and c_m is a mass flux coefficient defined by Eq. (3) of [7]. In all our tests, the specific heat ratio γ of the gas was 1.4, corresponding to air. The values of the other three modeling parameters are listed in Table 2 for the cases discussed in this report. The coefficient c_m was adjusted to the desired value by using appropriate orifices which were calibrated for c_m by the method used in [7,9]. Actually, c_m is generally somewhat dependent on the dimensionless pressure difference $(p_D-p)/p_D$, where p is the pressure at the vent exit. The value of c_m given in table 2 is a reference value corresponding to a dimensionless pressure difference of 1/3.

Table 1 shows that the proportions of System A are approximately similar to those of a single "cell" of a GE Mark III containment except that our

model has one instead of three horizontal vents. From Table 2 we see, furthermore, that comparisons number 1 and 2 also simulate the vent flow resistance, the submergence, and the dynamic blowdown conditions of the Mark III system approximately, although it should be noted that our experiments are done with a constant drywell pressure and not with a linearly increasing one as in the Mark III system. Comparisons 3 and 4 represent a rather low simulated submergence as compared with Mark III, and comparison 4 furthermore has a very low scaled vent flow resistance, lower than the minimum possible value of unity in a full-scale system.

3. RESULTS

Our main goal was to test whether the three different systems, with identical flow-wise dimensions but different transverse dimensions, would exhibit similar pool swell transients under similar dynamic conditions. Four sets of comparisons will be described here, labeled numbers 1 - 4. Table 2 gives the dynamic similarity parameters for each set. The differences in the four cases are in the dimensionless submergence (a geometric parameter), and in the dimensionless parameters p_D/p_w and $c_m\ (R\ T_D/g\ \ell_v)^{1/2}$ which define the dynamic driving conditions for the pool swell transient. The dimensionless wetwell pressure $p_w/\rho g \ell_v$ had the same value of 6.4 in all tests. The reasons for the choice of these particular values of the similarity parameters is apparent from the discussion in Section 4.

3.1 Pressure histories

The pressure histories in the pool turned out to be quite similar in the three systems, except for a superposed oscillatory component which apparently resulted from an induced pool vibration and was different in the three systems. This is shown in Figs. 3 and 4. The top trace in each oscillogram represents transducer no. 1 in Fig. 2, and indicates the pressure in the vertical pipe, just downstream of the orifice. This pressure rises rapidly to the drywell pressure as the vertical pipe pressurizes after valve opening (the roughly 30 ms risetime in Fig. 3 is due to this effect, and does not reflect the valve opening time, which was short) and stays there until the air enters the pool from the vent (vent clearing), at which time the pressure begins to decrease. In case 4, which had a large orifice, the pressure rose to the drywell pressure in about 10 msec, and thereafter showed a small sinusoidal component which apparently resulted from acoustic effects in the air-filled portions of the vertical pipe and the vent.

The bottom trace in the oscillograms represents transducer no. 2, which is located in the pool floor 1/4 of the system width from the wall with the vent.

Transducer no. 2 shows no pressure rise, except for an oscillatory component, until the vent clears. Shortly thereafter the pressure rises rapidly to a maximum value, and then drops as the bubble grows and the pool swells. The pressure histories from the other transducers in the pool

(transducers no. 3 and 4) were similar in structure to that shown by transducer no. 2.

The oscillatory component of the pressure at the submerged points appeared to be due to pool vibration which resulted from wall flexibility, and possibly also from air bubbles which had not been completely cleared from the pool. Fig. 5 indicates signals from an accelerometer mounted on the outside of the side window in System B, the center of the pane, together with $p_4(t)$. The accelerometer shows a peak reading which coincides with the peak in p_4, and contains two dominant frequencies, one which is about the same as the dominant frequency in p_4 (of the order of 6 ms period in the case shown) and another which is higher (of the order of 2 ms period). Fig. 5 (c) shows the response of transducer 2 when the side wall was tapped with a hammer. The same two dominant frequencies appear to be present. The higher frequency is of the order expected for the natural frequency of this window, estimated [11] as being between 1 and 2 ms in system B, depending on whether one assumed that the window was rigidly or simply supported at its edges (the water mass associated with one window was only about 1/4 that of the window, and hence the effective mass of the water was not important for purposes of rough estimation).

The pressure histories are of secondary interest in the present study because they appeared to be relatively insensitive to the details of the pool swell process, and were therefore not useful as indicators of pool swell similarity in the three systems (see Figs. 3 - 5). For that reason,

we did not concentrate on taking pressure data, nor did we attempt to systematically trace down the origin of the oscillations in the pressure histories. In Appendix A we do provide an approximate analysis, however, which suggests that the observed pressure oscillations are very roughly consistent with the observed wall accelerations if one assumes that both resulted from a common fluid-structure interaction.

3.2 Vent Clearing Times

The vent clearing time t_o is the period between the opening of the valve, when the water in the feed tube begins to move, and the time when air first enters the pool from the vent. This period was determined directly from the high-speed films. Table 3 lists the values obtained for the three systems in the various comparison tests. There is a judgemental error of about ± 3 ms in these figures, associated with the difficulty of determining the initiation time for the event from the films. The possible error due to errors in film speed was negligible, since the clearing time was determined directly from time markers on the film rather than by counting frames.

The vent clearing times generally tended to increase from system A to B to C. We attribute the differences in t_o to differences in the hydraulic loss coefficients for the vents in the three systems. The orifices at the tops of the vertical feed pipes of the systems were calibrated so as to ensure the same loss coefficient in all three systems

for the air flow in the entire feed pipe/vent pipe system, from the downcomer to the pool at the vent exit. No attempt was made, however, to ensure the loss coefficients for the vent pipes, which control the water outflow, were the same in all three systems. The vent flow Reynolds numbers for the water were high, of the order of 10^5, and it is likely that the differences were not due to Reynolds number effects, but resulted simply from the geometrical differences between the three systems. The geometrical differences are apparent from Fig. 1. If the vent system head loss coefficient is determined by geometry and is Reynolds number independent, then it should be the same in any given system, regardless of the dynamic driving conditions (drywell pressure, etc.). The simple vent clearing analysis in Appendix B shows that our results can be explained reasonably well if one makes this assumption.

Geometrical differences would also exist between a full-scale system and a distorted-geometry simulation of it. Hence, vent clearing time differences similar to the ones observed here may also be found between full scale systems and their distorted-geometry simulations.

3.3 Pool Swell

Figs. 6 to 24 show comparisons of the pool profiles in the three systems at various times after vent clearing. The figures are views of the broad side of the systems, showing the apparent profiles of the top water surface and the air-water interface of the bubble which emerges from the horizontal vent. They

were traced directly from projections of the high-speed films. The line boundaries are visual approximations. The time t_o was determined to an accuracy of ± 3 ms, and $t - t_o$, which was obtained by counting film frames, is accurate to better than ± 5%.

Some of the figures also indicate the location of the starting vortex. This is the ring vortex which forms when the vent flow begins, and then moves into the pool. The vortex was often visible in the films, presumably because it contained cavitation bubbles in its core.

Figs. 25 to 28 show the histories of maximum pool surface elevation and maximum bubble elevation for the four comparison cases.

It is apparent from Figs. 6 to 24 that three-dimensional effects are present and cause differences in the pool profiles between all three systems, the differences being more profound between systems A and B than between B and C. System A tends to have an earlier breakthrough than system B and C, and the water ligament tends to be thinner at the top of the pool and the ligament (or surface) velocity higher (see also Figs. 25 to 28).

The data shown in Figs. 6 to 28 should be viewed as containing some uncertainty since the pool histories contained an element of randomness. The degree of that randomness is illustrated in Figs. 29 to 31, which show the results from three repeated runs in the same system at identical operating conditions. Note that error the in t_o is better than ± 3 ms, and the error in $t - t_o$ is below ± 5%. The randomness appeared to be largest when the submergence was small, as in the example, and pool breakthrough occurred early.

Surface tension effects did not appear to play a dominant role in the pool swell process before pool breakthrough. Fig. 32 shows one of the test cases which were run with and without detergent in the pool water. The difference in the cases is insignificant, less than the scatter observed in Fig. 31 (the smaller scatter is likely due to the larger submergence, and later breakthrough).

The dominant three-dimensional features of the pool, which are quite apparent in all tests in system A, appear to be imprinted by the interaction between the starting vortex and the bubble. The starting vortex is generated at the vent exit when the vent clearing process begins. After the vortex is formed, which takes a time about equivalent to the ejection of 2-3 vent diameters of water [12], it propels itself into the pool at a speed less than 1/2 that of the water jet emerging from the vent (the vortex speed is of the order of 1/2 the jet speed in an unconfined situation, but in this case the side walls have the effect of reducing the vortex convection speed below that value). The leading edge of the bubble emerges at essentially the water outflow speed at the instant of clearing (see Appendix B), and begins to overtake the slower-moving vortex (see Fig. 6, for example, or Fig. 11). If the pool is wide enough, the vortex will be overtaken before it reaches the opposite wall. The circulatory flow field of the vortex first speeds up the tip of the bubble as it closes in on the vortex, creating a necking-down effect (Fig. 12, for example), and then the bubble is convected outward as it reaches the other side of the vortex, and a mushroom-shaped

tip results (see Fig. 12, or Fig. 7, for example). This characteristic shape is retained through the rest of the pool swell (see Figs. 13-15, for example). The rate of advance of the leading edge of the bubble tends to slow somewhat after it penetrates the vortex (see Figs. 33 and 34). This may be due more to the fact that the bubble is approaching the opposite wall than to the effect of the vortex interaction, however.

When the system width is too small for the bubble to be able to overtake the vortex before it approaches the other side, the bubble penetrates the pool more uniformly and three-dimensional effects are less prominent in the pool. This was the case in systems B and C in most of the present tests. A comparison of cases 1 to 4 shows, however, that the degree of the differences between systems A and B (and to a lesser extent, between B and C) appear to depend not only on how fast the bubble catches up with the starting vortex, but also on other dynamic factors such as the drywell pressure (p_D/p_w), the enthalpy flux ($c_m\sqrt{RT_D/g\ell_v}$), and the initial submergence (s/ℓ_v).

4. DISCUSSION AND CONCLUSIONS

The comparisons described here show that the reduction of flow cross-sectional areas by a factor of 3 can cause significant differences in a typical pool swell process in a simulated horizontal-vent containment system. The degree of the difference depends on both system geometry (c.f. the substantial differences between systems A and B, and the relatively small

differences between systems B and C), submergence (greater difference at lower submergence), and the dynamic driving conditions (higher enthalpy flux tends to cause more severe differences, for example, and lower drywell pressure appeared to increase the differences, at least in the cases examined here). The causes of the differences are too complex and subtle to allow any general conclusions about the accuracy of distorted-geometry tests to be drawn from the data generated in this particular study. We are not in a position to offer a general criterion for when a distorted-geometry tests will, or will not, be a reasonably accurate simulation.

The systems tested in this study were roughly similar, however, to a single cell of the Mark III containment. Table 1 shows that the geometrical features of system A were approximately similar to the full-scale Mark III system, Systems B and C would then correspond to "1/3-scale" and "1/9-scale" distorted-geometry representations (by area). There was, however, an important difference between our systems and the Mark III: ours had a single horizontal vent, while the Mark III has three vents arranged one above the other.

The dynamic conditions (see Table 2) were also approximately similar to those in the Mark III, although no attempt was made for an exact simulation. The drywell pressure in our system was constant (or applied as a step-function, as it were) after the initiation of the event, at a value of either two or three times p_w. In the Mark III, the drywell pressure increases approximately linearly from about p_w after the initiation of the

event to a value two or three times higher than p_w. In our system the enthalpy flux simulation parameter $c_m(RT_D/g\ell_v)^{1/2}$ had a value of 22 in Cases 1-3, and a value of 62 in Case 4. A full scale plant, with a full scale ℓ_v = 1.5m, would have a value $c_m (RT_D/g\ell_v)^{1/2}$ = 22 if it's vent flow resistance (1 + $f\ell/d$) were 4.6 (see Table 2). This resistance value of 4.6 is roughly representative of a Mark III system. The enthalpy flux parameter of 62 in Case 4 would imply a full-scale vent flow resistance (1 + $f\ell/d$) of 0.6, which is smaller than the lowest possible value of 1. Thus, this case simulates an enthalpy flux which is, as it were, an upper bound on physically possible values in any full-scale system.

The dimensionless submergences of s/ℓ_v = 1.67 in Cases 1 and 2 would scale up to a submergence of 8.2 ft. in a full-scale plant with ℓ_v = 1.5m (Table 2). This is a fairly representative value. The Case 3 and 4 submergences of s/ℓ_v = 1.00 would imply a 5 ft. full scale submergence, which is lower than suggested for Mark III use.

In summary, then, Cases 1 and 2 have dynamical conditions and submergences reasonably representative of those in Mark 3, while Case 3 has a low submergence, and Case 4 has both a low submergence and too high an enthalpy flux. System A is roughly similar to a single cell of a Mark III, and systems B and C are 1/3-scale and 1/9-scale (by area) distorted-geometry representations, respectively. Note, however, that the similarities are <u>not exact</u>. There are important differences: our systems have a single

horizontal vent, not three, and our drywell pressures are applied in a step-function manner, and not as a linear rise from p_w.

Insofar as our Cases 1 and 2 are similar to the Mark III systems, we can conclude the following:

(1) There are significant three dimensional differences in the pool profiles between system A (representing the full-scale system) and its "1/3-scale" counterpart, system B. See Figs. 6-15. The "1/9-scale" system (system C) behavior is much closer to that of the "1/3-scale" than the "1/3-scale" is to the "full-scale".

(2) Pool breakthrough occurs considerably earlier in the "full-scale" system than in its "1/3-scale" or "1/9-scale" counterparts. This is apparent in Figs. 25-28. In Case 2 (Fig. 26), the water ligament thickness is reduced to about 0.1s after a rise by about 1.3s in system A. This water ligament thickness is not attained until the surface has risen by more than 2s in systems B and C (the precise level lies outside the data base). In Case 1 (Fig. 25), breakthrough occurs in System A near the point when the water reaches the ceiling, a rise of 2s. At the same level, systems B and C are still far from breakthrough. The differences are even more pronounced in Cases 3 and 4 which are not, however, as representative of Mark III as Cases 1 and 2.

(3) The relatively thinner water ligament in the "full-scale" system causes a higher maximum pool rise velocity in that system than in its "1/3-scale" and "1/9-scale" counterparts, at least at times nearing breakthrough (See Figs. 25 and 26). We are not in a position to make general statements about the amount of the difference, as it appears to be rather sensitive to the dynamic conditions as well as to the submergence.

One of the more interesting general conclusions that emerges from our study is that the vent clearing process plays a significant role in determining the shape of the bubble and the pool surface during the pool swell process, at least if the pool is wide enough, as in system A. It does so via the starting vortex which is generated in the early moments of vent flow initiation. When the bubble emerges, it travels into the pool at a speed higher than the vortex which preceded it (see Appendix B, and Figs. 33 and 34), and, if the pool is wide enough (as in our system A), overtakes the vortex. The interaction of the bubble with the vortex imprints a mushroom shape on the leading side of the bubble, and this basic shape is retained, with small modifications, throughout the pool swell process.

Clearly, any numerical code for computing the three dimensional features of this kind of pool swell process is doomed to failure unless it is capable of dealing accurately with the formation of the starting vortex and its induced pool velocity field.

REFERENCES

1. J.E. Torbeck, D.L.Galyardt, J.P. Walker, "Mark I 1/12-Scale Pressure Suppression Pool Swell Tests", GE Report NEDE-13456, 1976.

2. D.L. Galyardt, C.G. Hayes, S.L. Kushman, "Mark I Containment Program 1/4-Scale Pressure Suppression Pool Swell Test Program: Scaling Evaluation", GE Report NEDO-21627, 1978.

3. E.W. McCauley, J.H. Pitts, et al., "Final Air Test Results for the 1/5-Scale Mark I Boiling Water Reactor Pressure Suppression Experiment", Lawrence Livermore Laboratory Report UCRL-52371/NUREG/CR-0151, 1977.*

4. R.L. Kiang and B.J. Grossi, "Three Dimensional Pool Swell Modeling of a Mark I Suppression System", EPRI Report EPRI NP-906, 1978.

5. R. L. Kiang and B.J. Grossi, "Dynamic Modeling of a Mark II Pressure Suppression System", EPRI Report EPRI NP-441, 1977.

6. F.J. Moody, "A Systematic Procedure for Scale-Modeling of Problems in Unsteady Fluid Mechanics", GE unpublished report, 1976. (Available from GE, 175 Curtner Ave., San Jose, Calif. 95114).

7. W.G. Anderson, P.W. Huber, A.A. Sonin, "Small Scale Modeling of Hydrodynamic Forces in Pressure Suppression Systems", U.S. Nuclear Regulatory Commission Report NUREG/CR-0003, 1978.*

8. A.A. Sonin and P.W. Huber, "On the Scaling Laws for Air Clearing in Water-Type Pressure Suppression Systems", J. Heat Transfer, 100, 601-604, 1978.

9. W.G. Anderson, P.W. Huber, A.A. Sonin, "Experimental Tests of the Scaling Laws for Air Clearing in Water-Type Pressure Suppression Systems", J. Heat Transfer, 100, 605-612, 1978.

10. R.J. Ernst, T.R. McIntyre, L.L. Myers, J.E. Torbeck, "Mark III Confirmatory Test Program One-Third Scale Three-Vent Tests", GE Report NEDM-13407, 1975.

11. C.M. Harris and C.E. Crede, editors, "Shock and Vibration Handbook", Vol. 1, McGraw-Hill, New York, 1961, Chapter 7.

12. T. Maxworthy, J. Fluid Mechanics, 81, 465-495, 1977.

*Available for purchase from the NRC/GPO Sales Program, U.S. Nuclear Regulatory Commission, Washington, D.C. 20555, and the National Technical Information Service, Springfield, Virginia 22161.

TABLE 1: GEOMETRICAL PARAMETERS

	Small-scale systems			Mark III
	A	B	C	
Vent length	9 cm	9 cm	9 cm	1.5 m
Pool width	39 cm	22.5 cm	13 cm	5.8 m
$\frac{\text{Pool width}}{\text{Pool breadth}}$	3.0	3.0	3.0	2.5
$\frac{\text{Vent diameter}}{\text{Pool width}}$	0.10	0.10	0.10	0.12
$\frac{\text{Vertical pipe area}}{\text{Pool Area}}$	0.053	0.053	0.053	0.08
$\frac{\text{Pool width}}{\text{Vent length}}$	4.33	2.5	1.44	3.9

TABLE 2: OPERATING CONDITIONS

1	2	3	4	5	6	7	8
SMALL-SCALE TEST CONDITIONS						CORRESPONDING MARK III FULL SCALE CONDITIONS	
	Test Conditions		Scaling Parameters				
Comparison No.	C_m	Submergence (cm)	$\frac{\text{Submergence}}{\text{Vent Length}}$	$C_m\sqrt{\frac{RT_D}{g\ell_v}}$ (1)	$\frac{P_D}{P_w}$	Mark III Submergence corresp. to Column 4	Mark III vent resistance $(1+\frac{f\ell}{d})$ corresp. to Column 5 (2)
1	0.07	15	1.67	22	3.0	2.5m (8.2 ft)	4.6
2	0.07	15	1.67	22	2.0	2.5m (8.2 ft)	4.6
3	0.07	9	1.00	22	3.0	1.5m (4.9 ft)	4.6
4	0.20	9	1.00	62	3.0	1.5m (4.9 ft)	0.6

(1) $\ell_v \equiv$ vent length

(2) Based on relation $(1 + \frac{f\ell}{d}) = C_m^{-2}$; T_D was computed on the assumption that the drywell air is compressed isentropically by a pressure ratio of 2, starting from a temperature of 300 K.

For all small-scale tests, $P_w/\rho g\ell_v = 6.4$ ($P_w = 5.67$ kPa)

For Mark III conditions, $P_w/\rho g\ell_v = 6.8$

TABLE 3: EXPERIMENTAL VENT CLEARING TIMES t_o

Comparison no.	t_o , ms.		
	System A	System B	System C
1	112	115	145
2	154	179	182
3	70	82	96
4	74	85	89

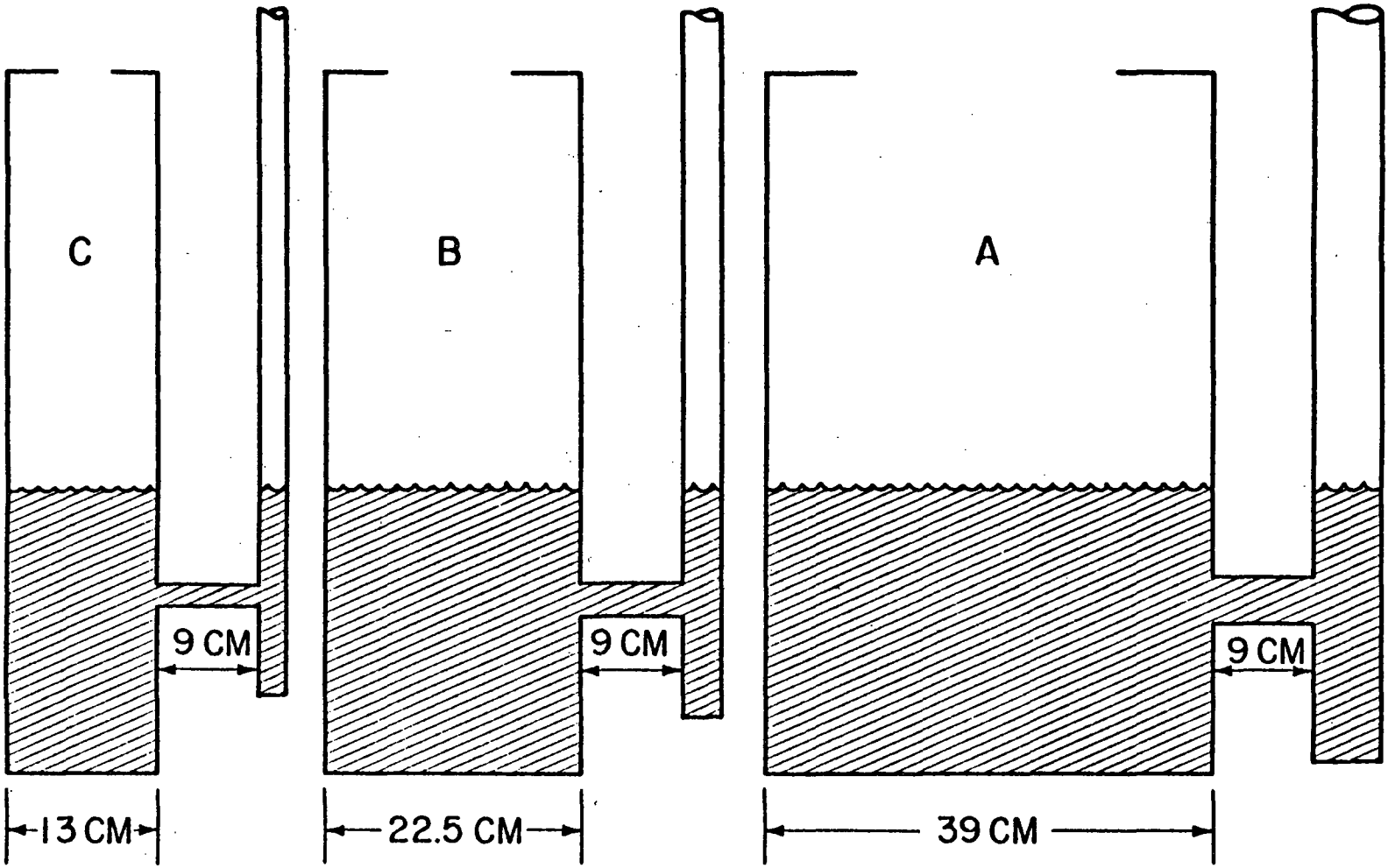

Figure 1: Systems A, B and C, side view.

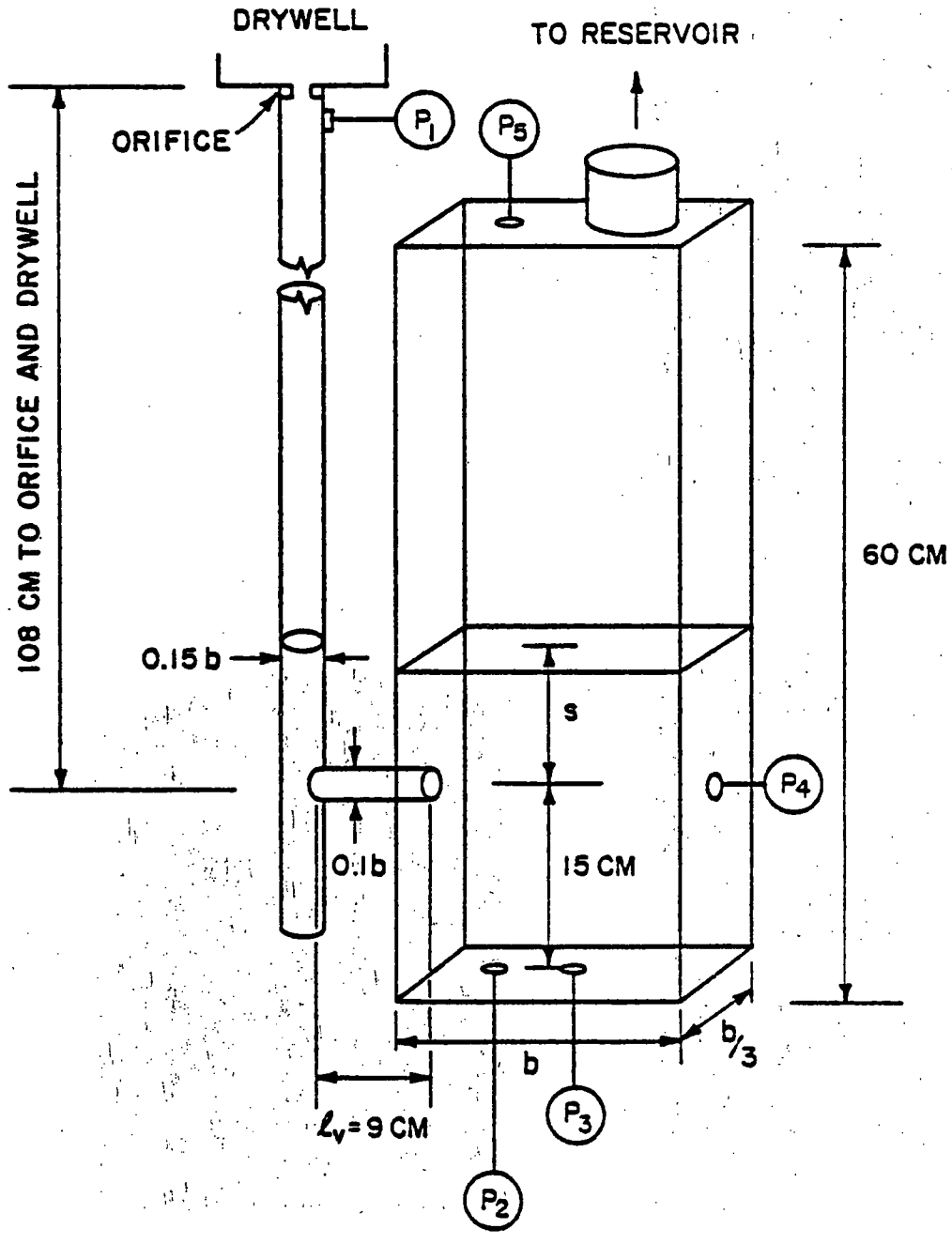

Figure 2: Proportions of systems A, B and C.

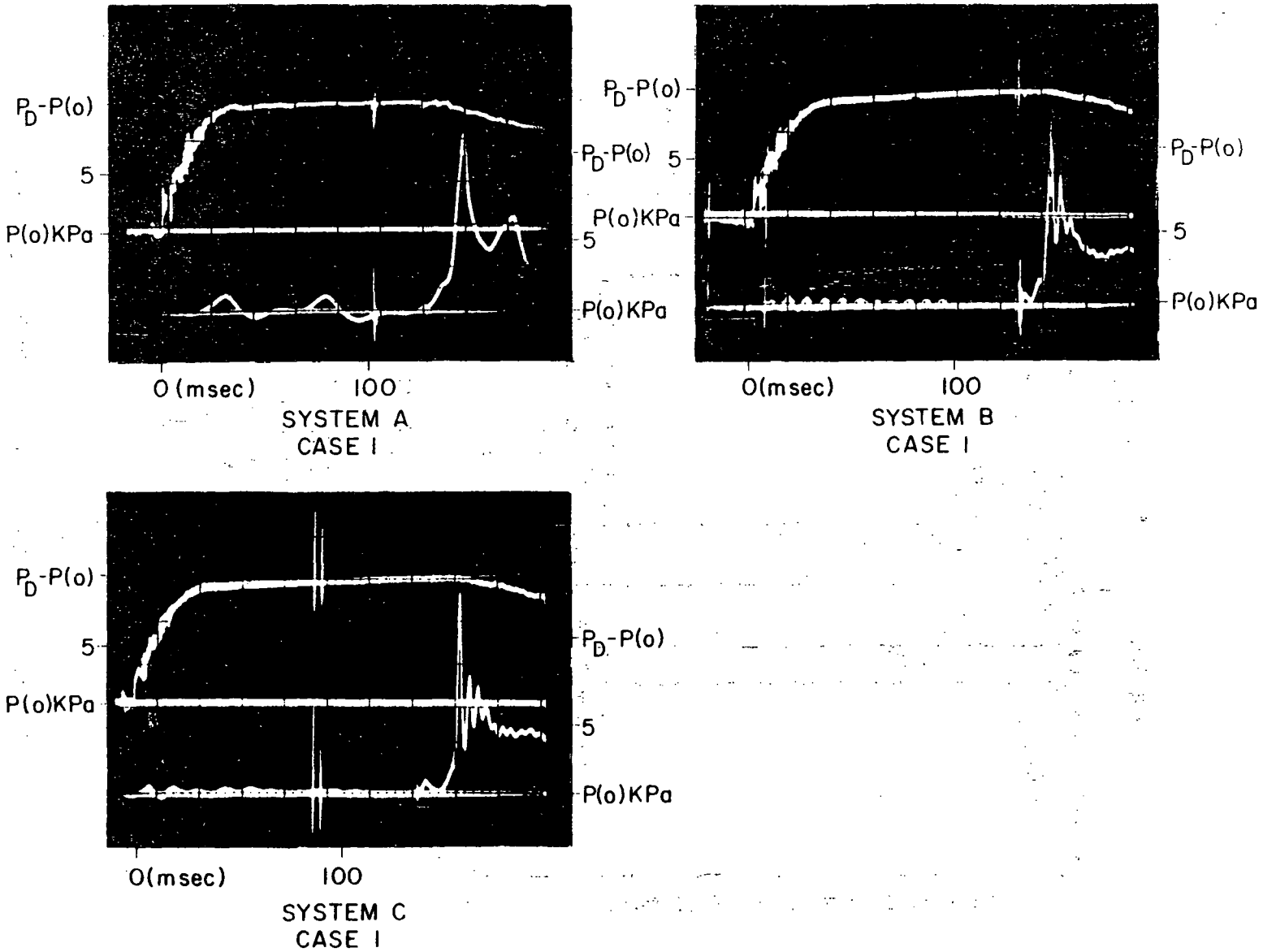

Figure 3: Case 1, p_2 vs time for systems A, B and C.

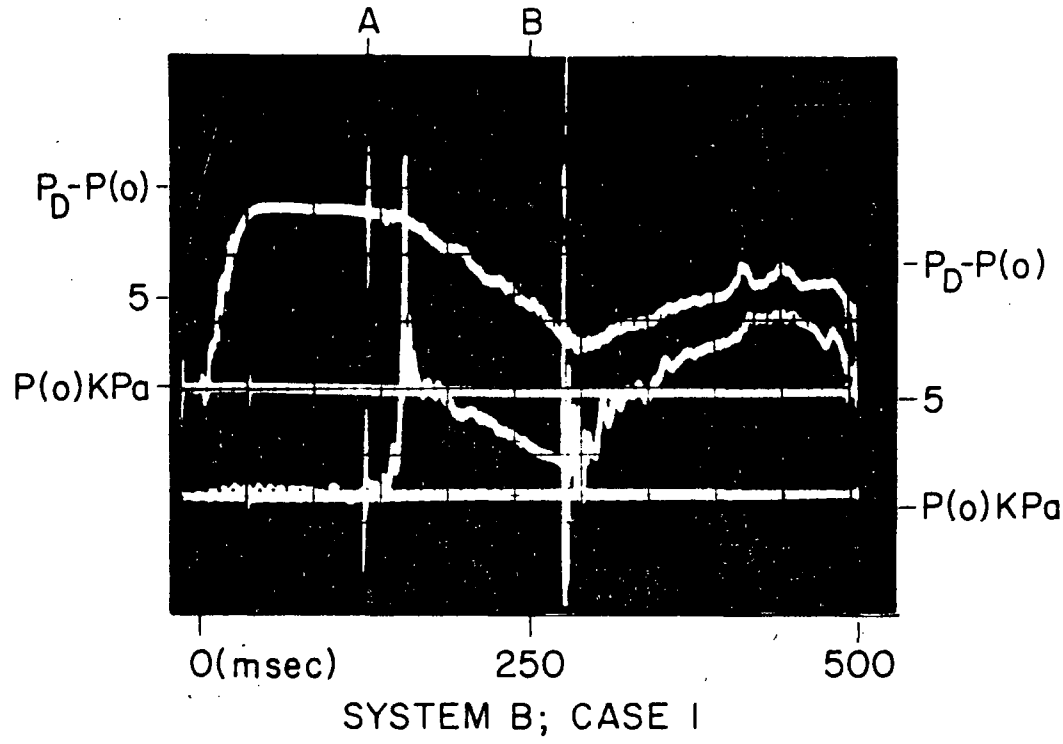

SYSTEM B; CASE I

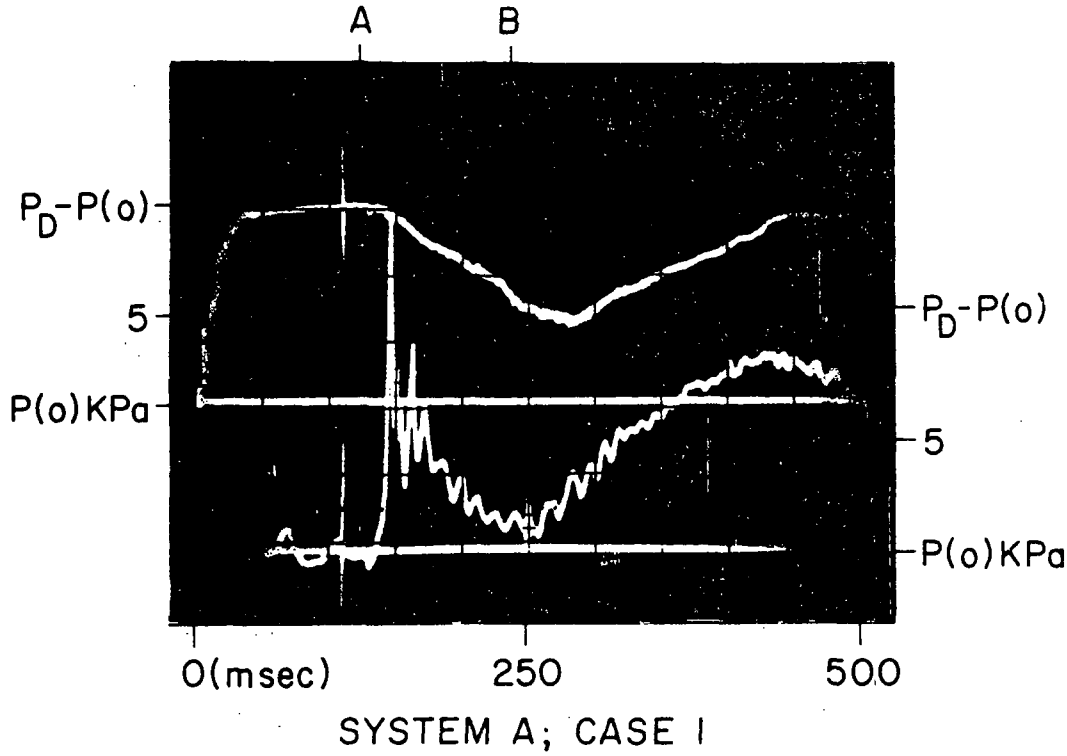

SYSTEM A; CASE I

Figure 4: Case 1, p_2 vs time for systems A and B, including long-time behavior.

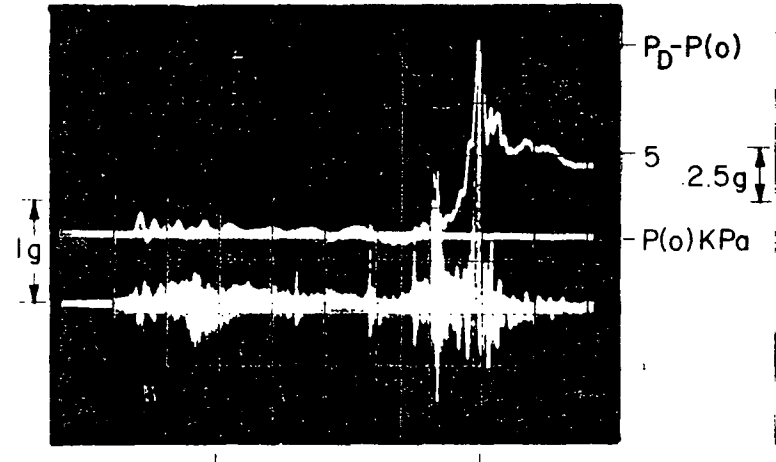

SYSTEM B; CASE 1
FLOOR TRACE
ACCELEROMETER

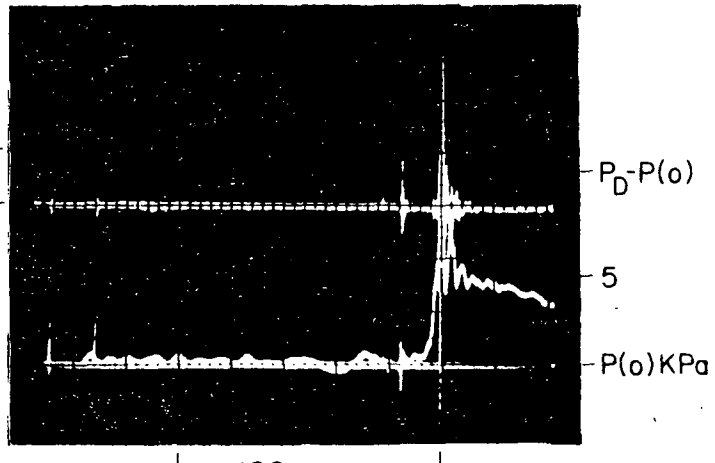

SYSTEM B; CASE 1
ACCELEROMETER
FLOOR TRACE

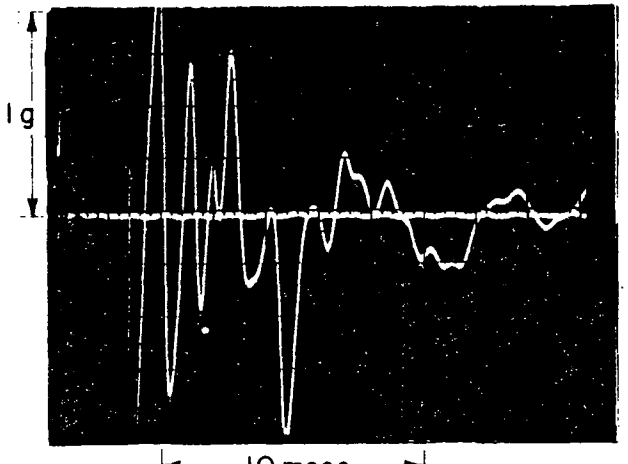

SYSTEM B
ACCELEROMETER TRACE
IMPULSE LOADING ON FRONT WALL

Figure 5: p_2 and, window acceleration versus time in Case 1, system B. Also, window acceleration versus time resulting from tapping window with hammer.

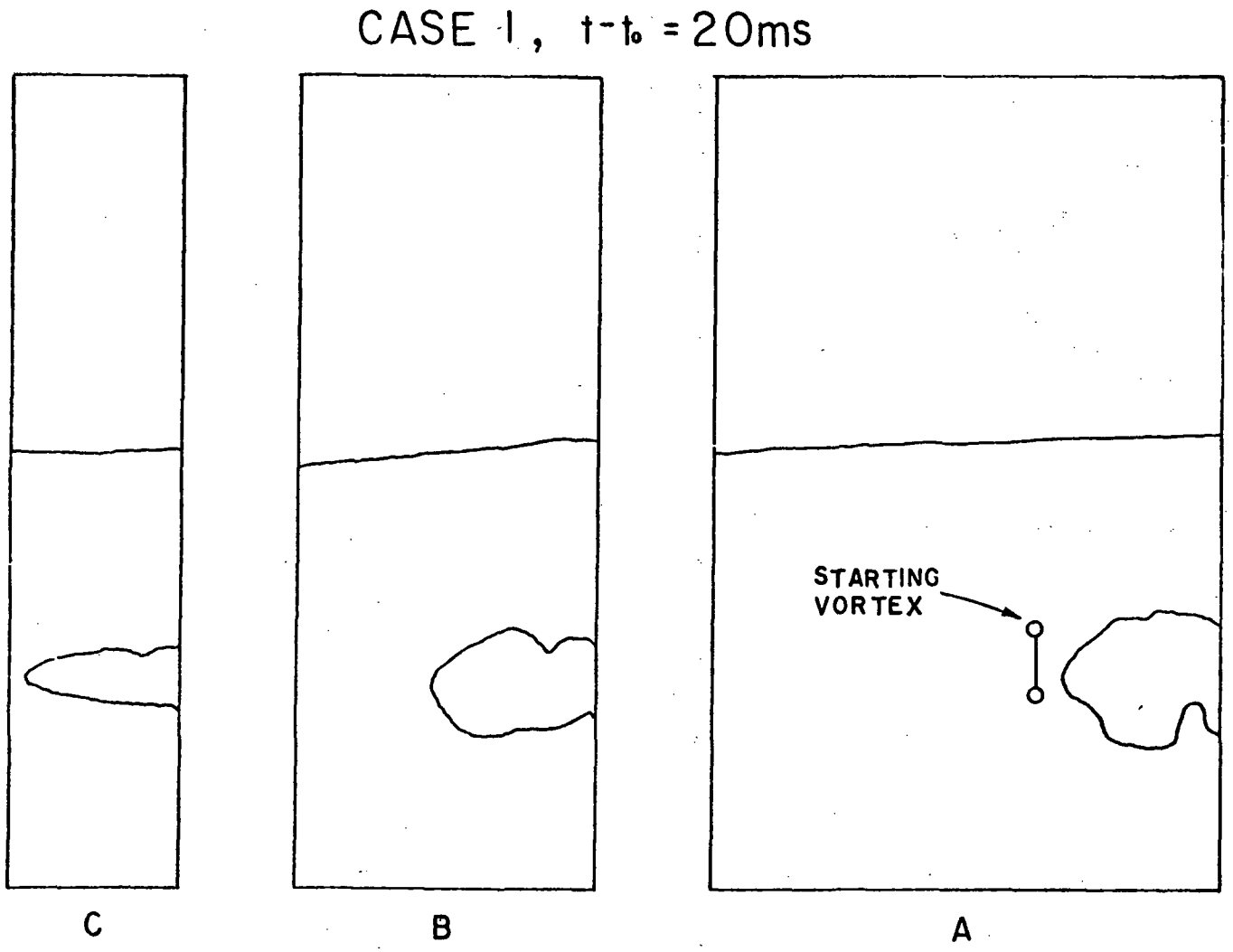

Figure 6: Case 1 at $t-t_o$ = 20 ms.

CASE 1, $t-t_o = 36$ ms

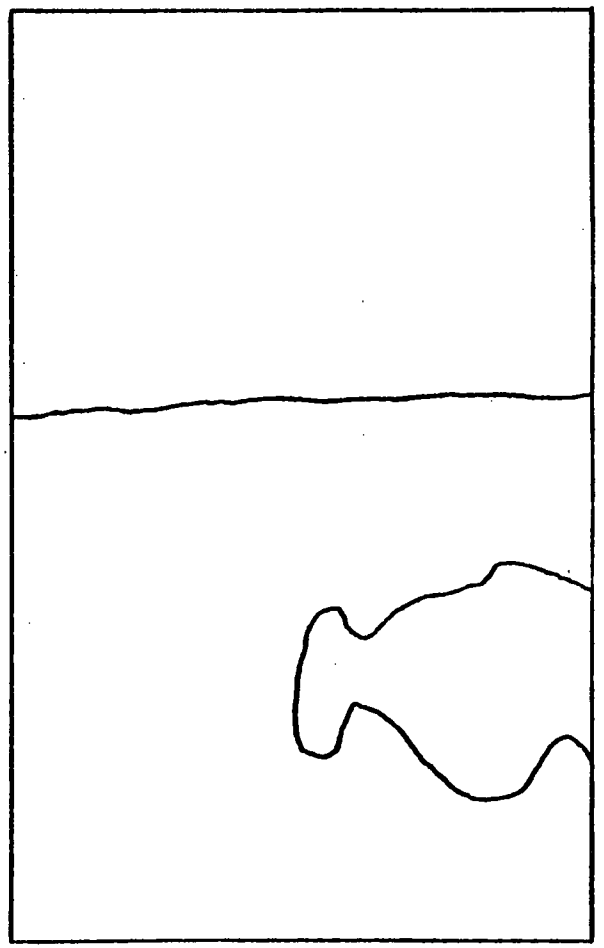

Figure 7: Case 1 at $t-t_o = 36$ ms.

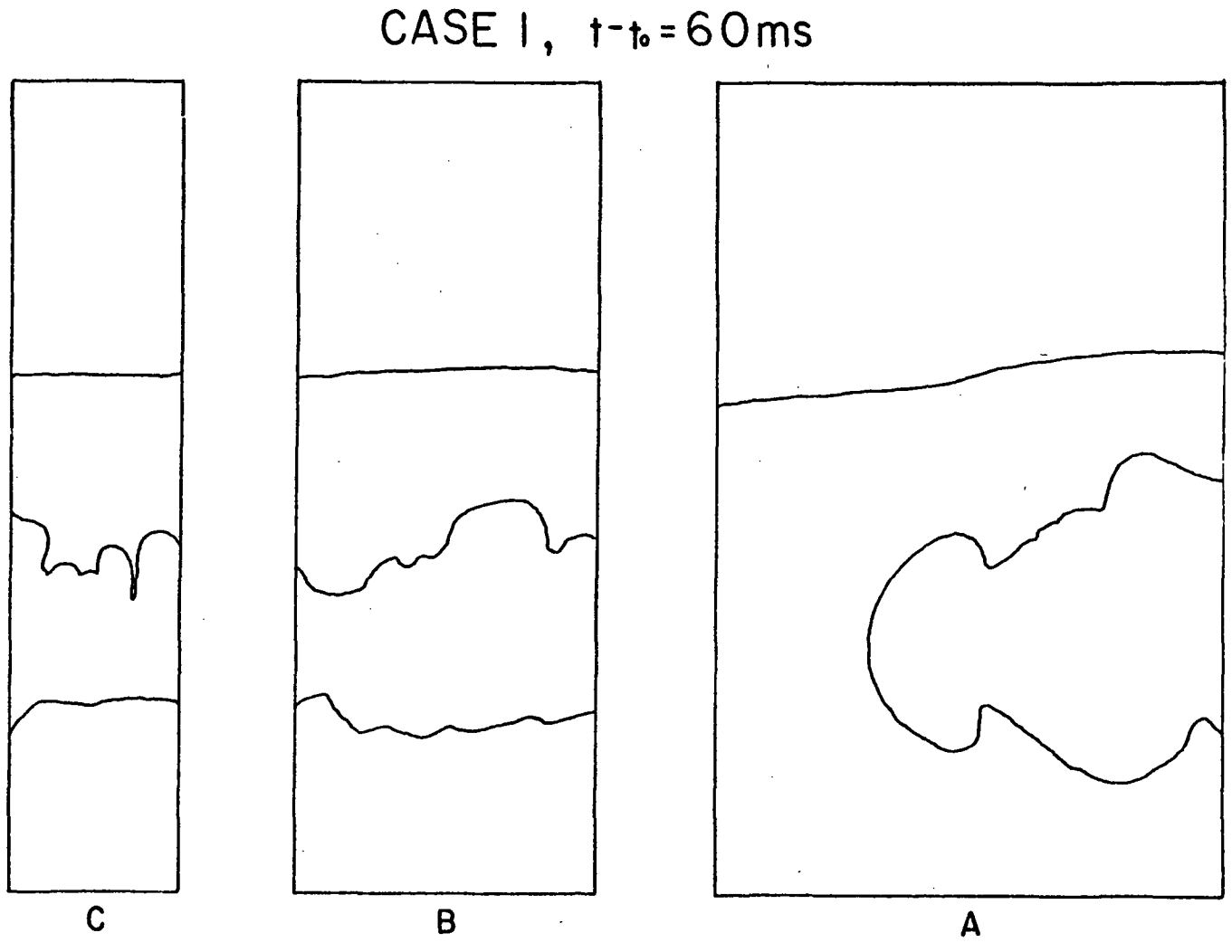

Figure 8: Case 1 at $t-t_o$ = 60 ms.

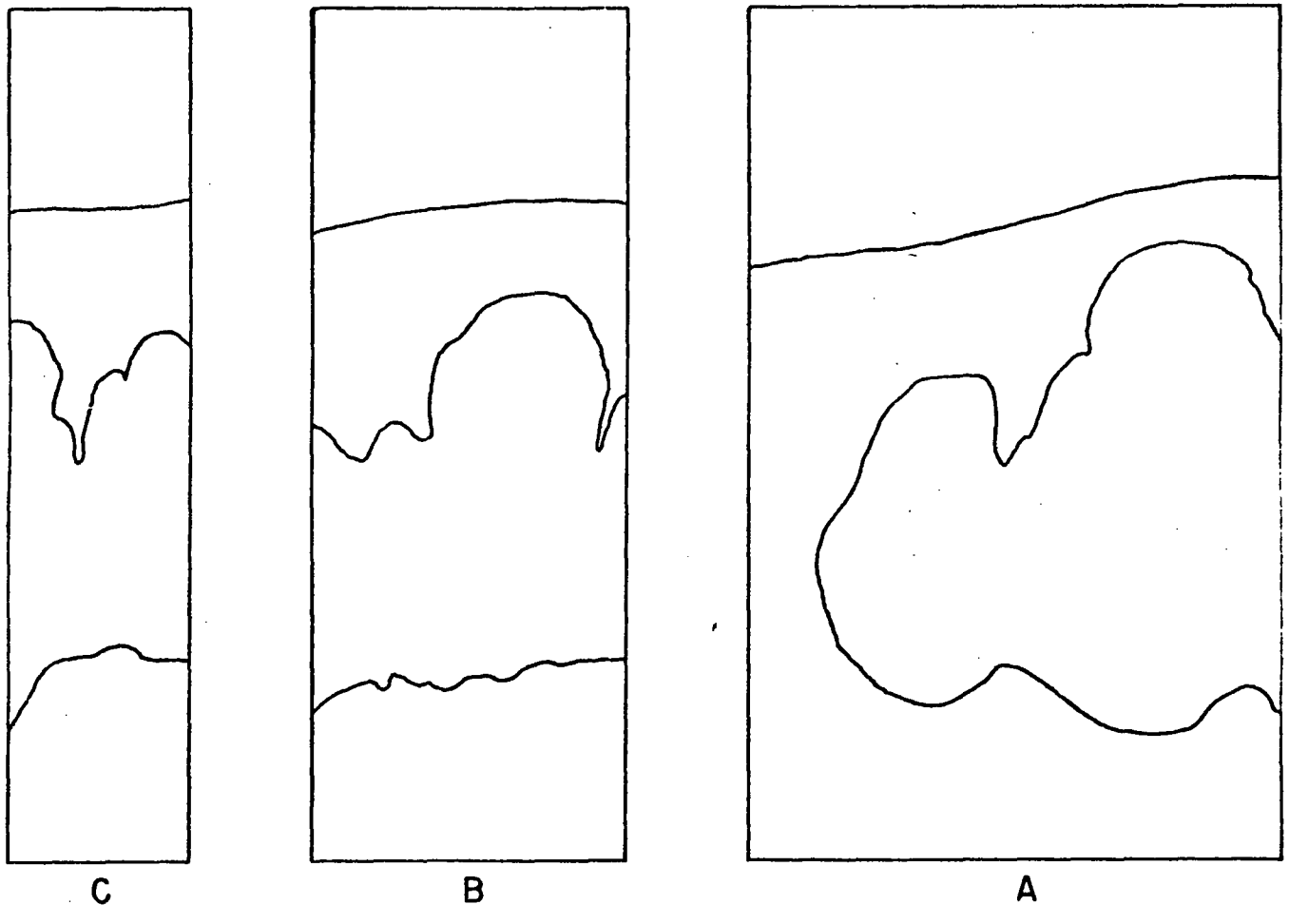

Figure 9: Case 1 at $t-t_o$ = 90 ms.

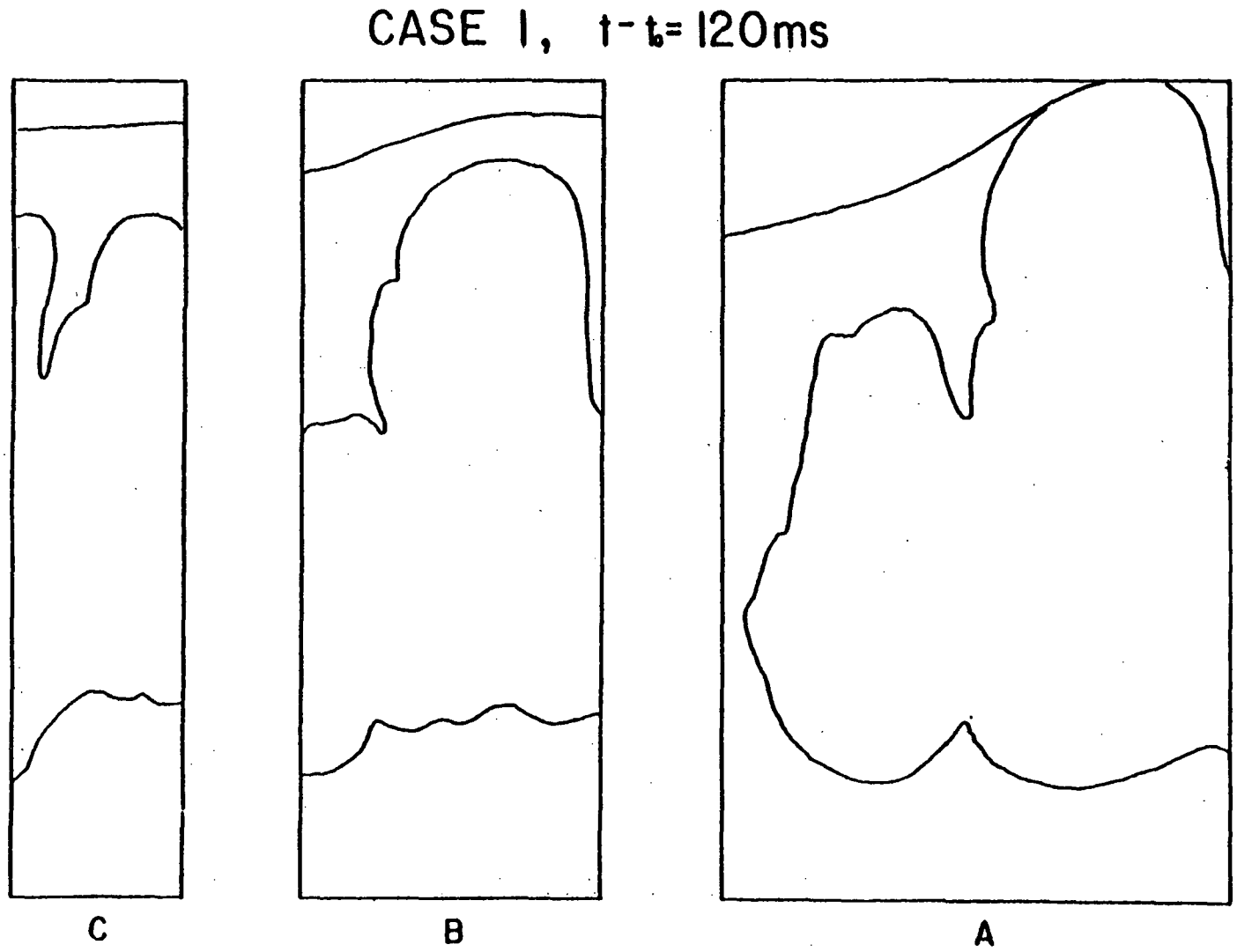

Figure 10: Case 1 at $t-t_0$ = 120 ms.

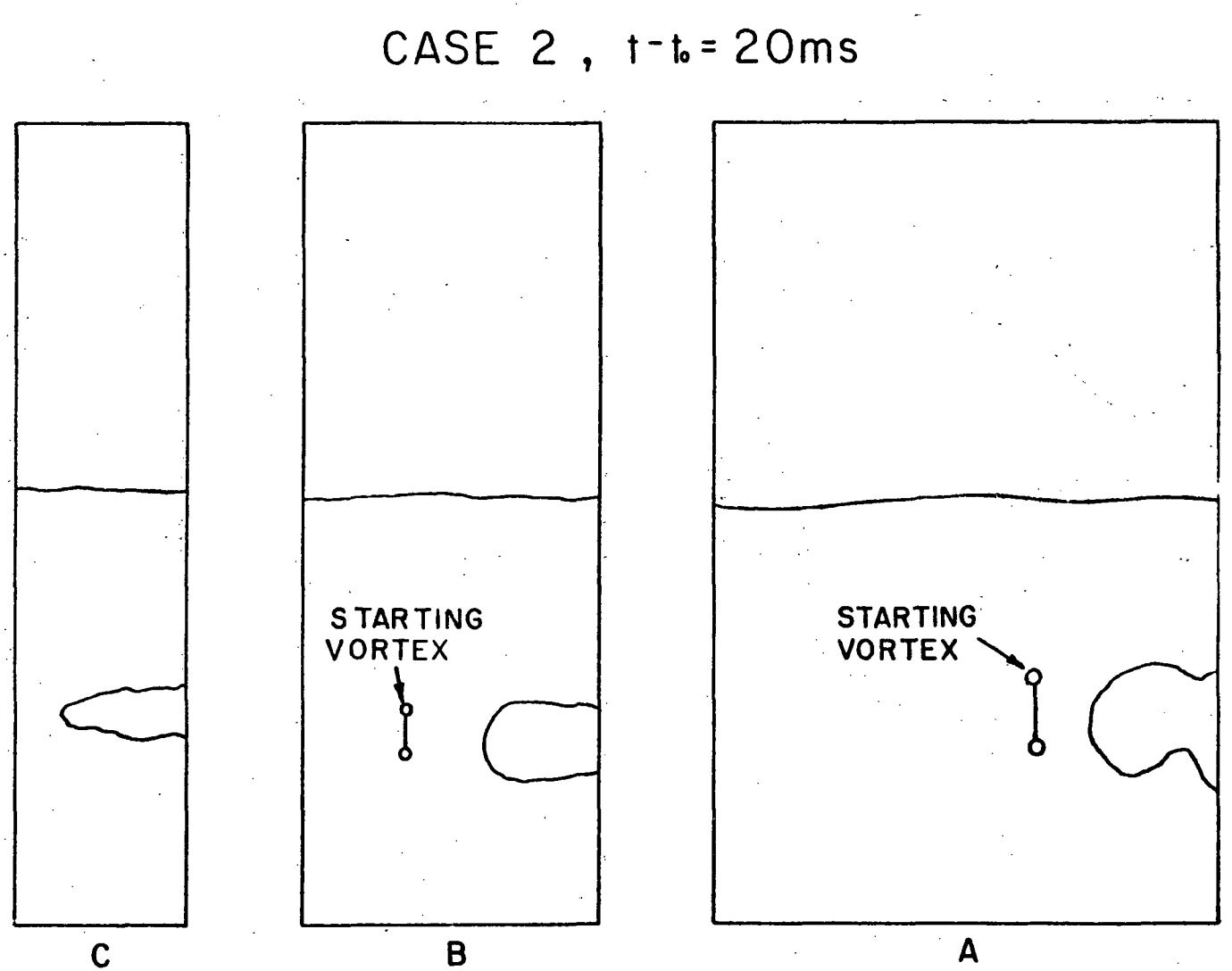

Figure 11: Case 2 at $t-t_o$ = 20 ms.

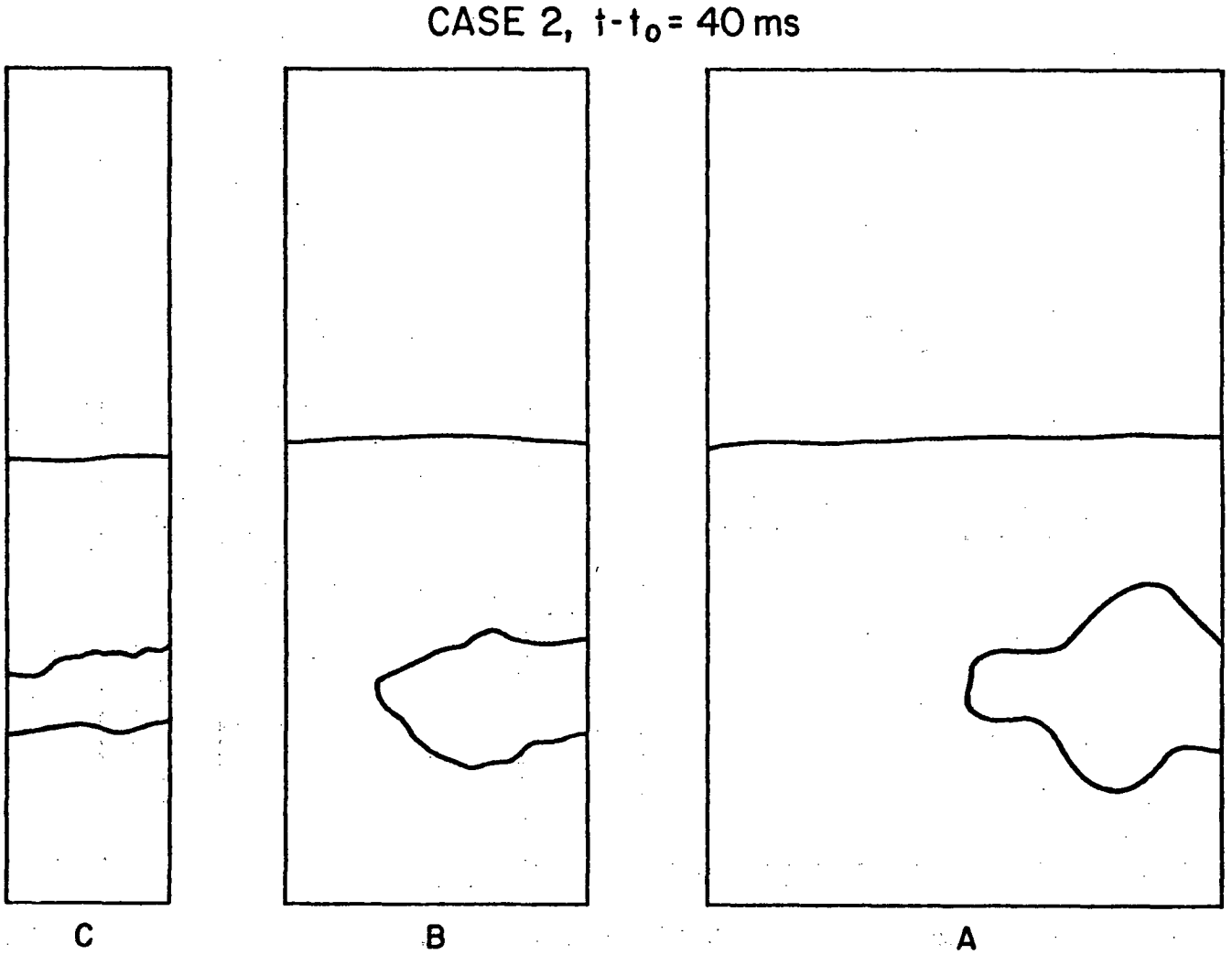

Figure 12: Case 2 at t-t$_o$ = 40 ms.

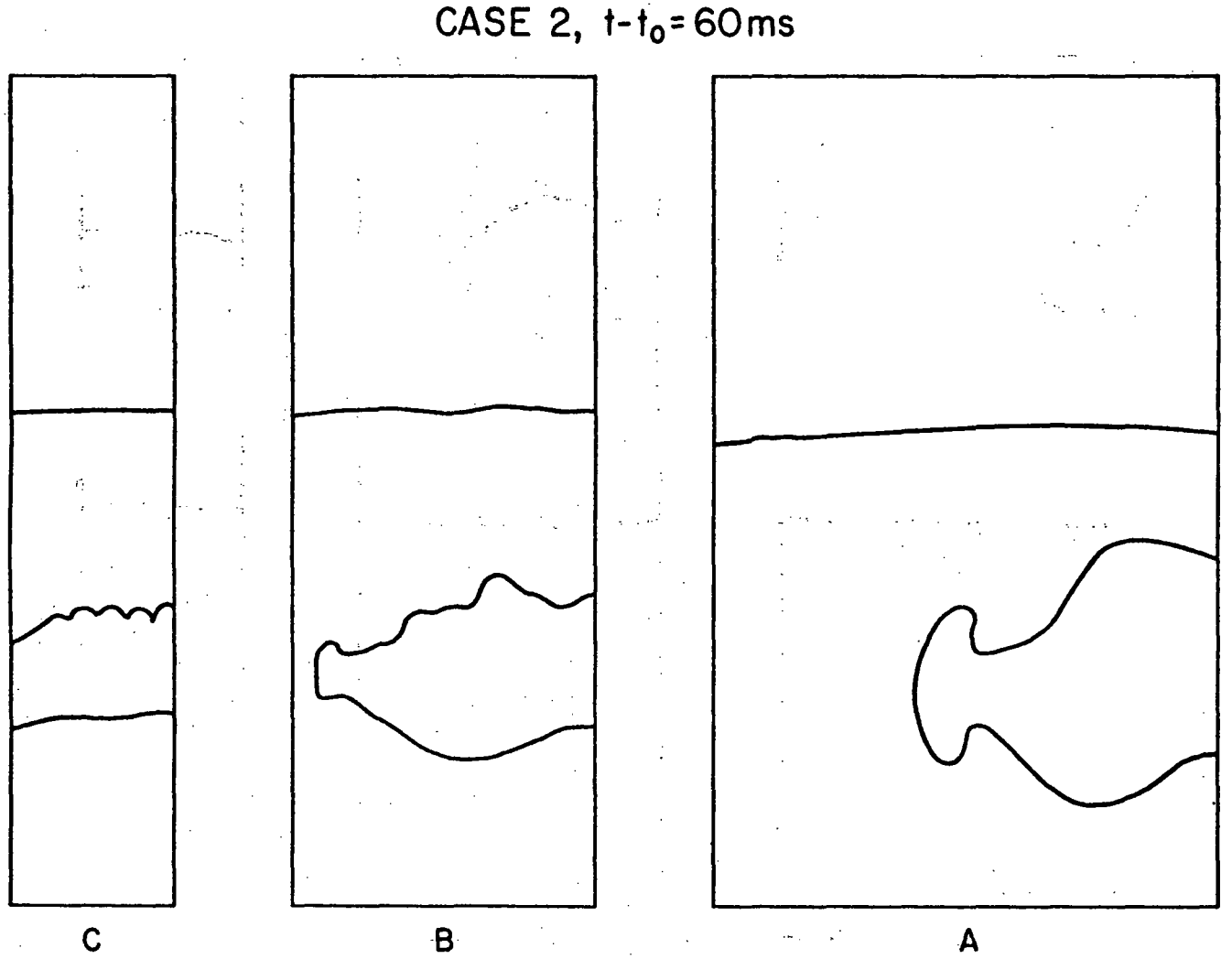

Figure 13: Case 2 at t-t_o = 60 ms.

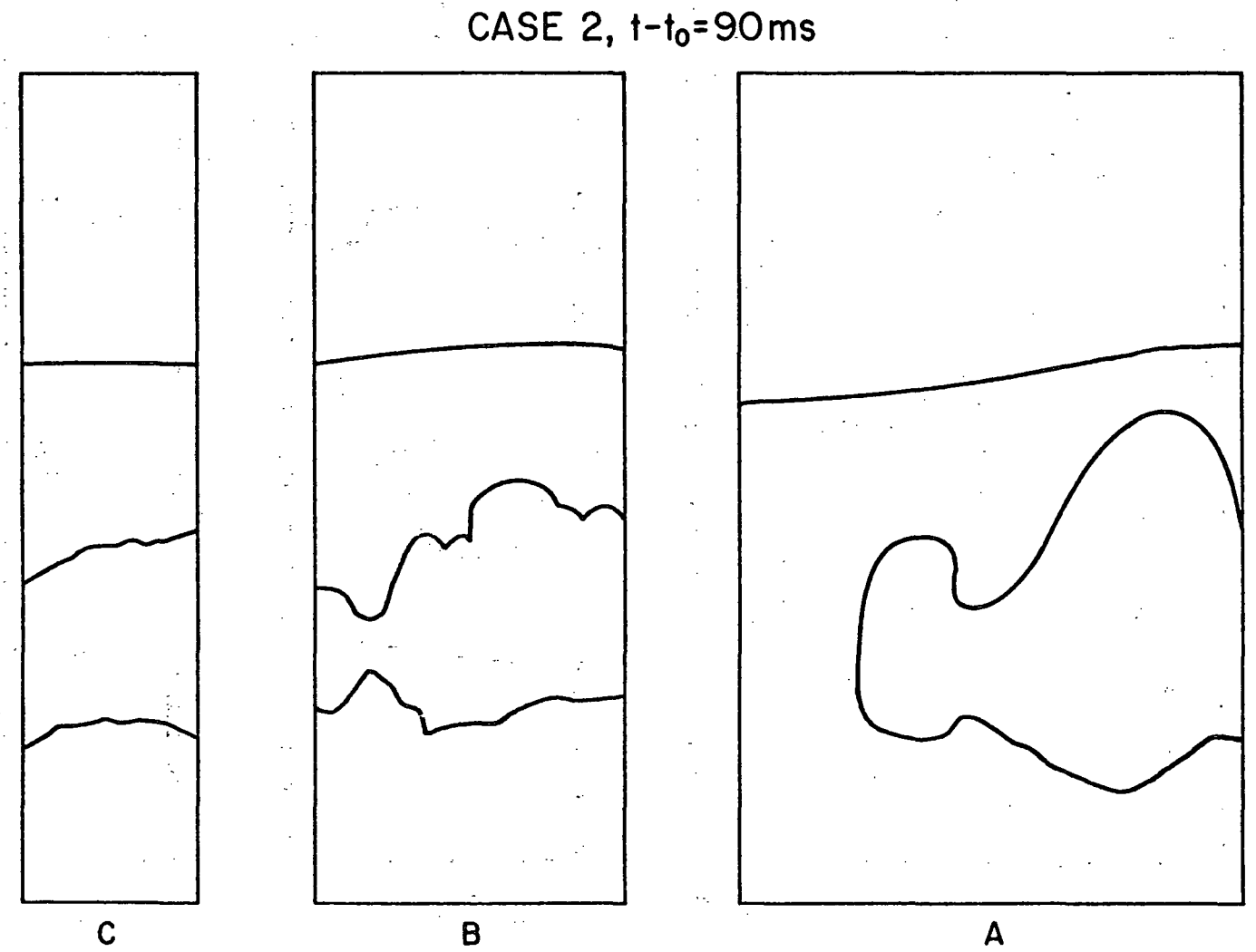

Figure 14: Case 2 at $t-t_o$ = 90 ms.

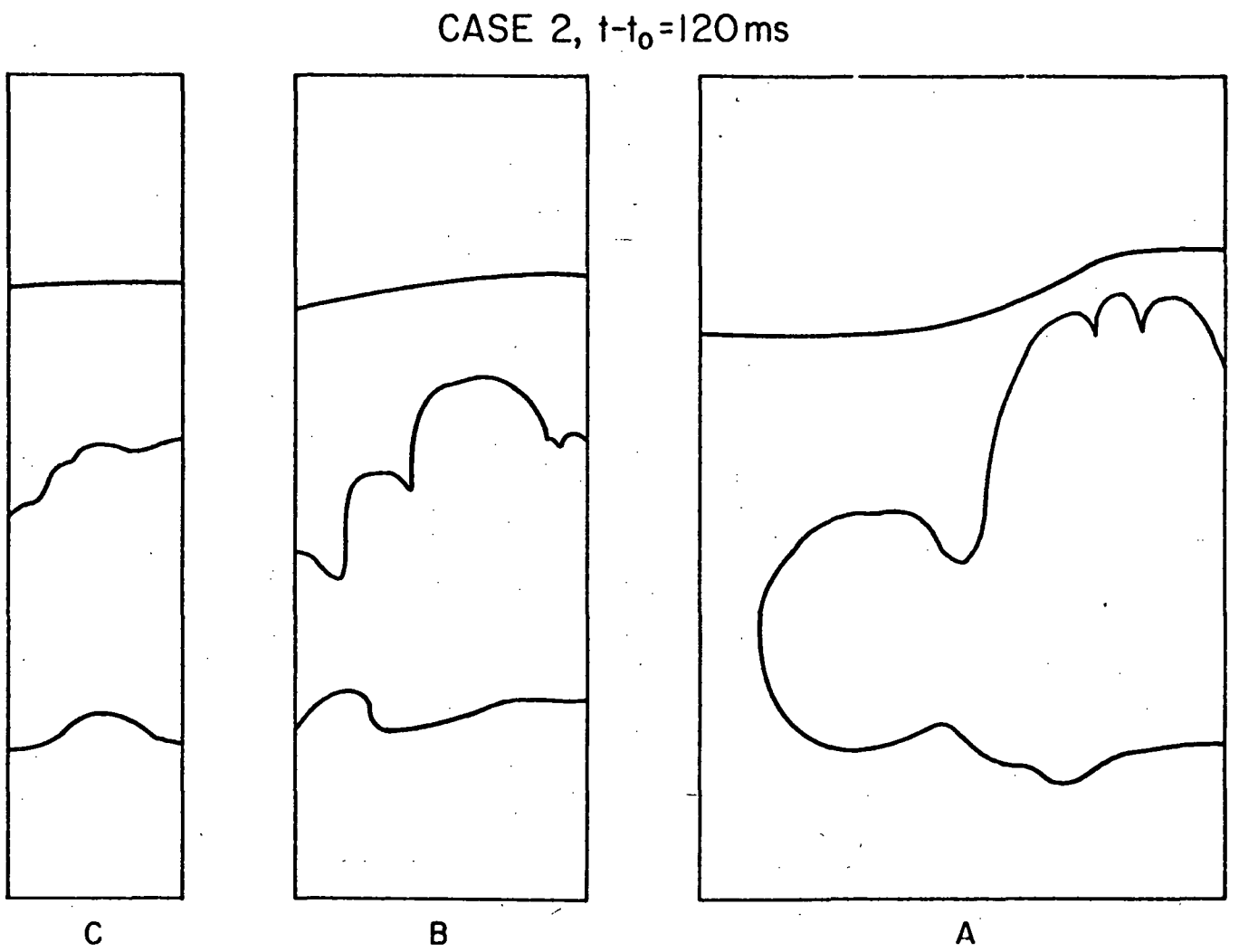

Figure 15: Case 2 at $t-t_o$ = 120 ms.

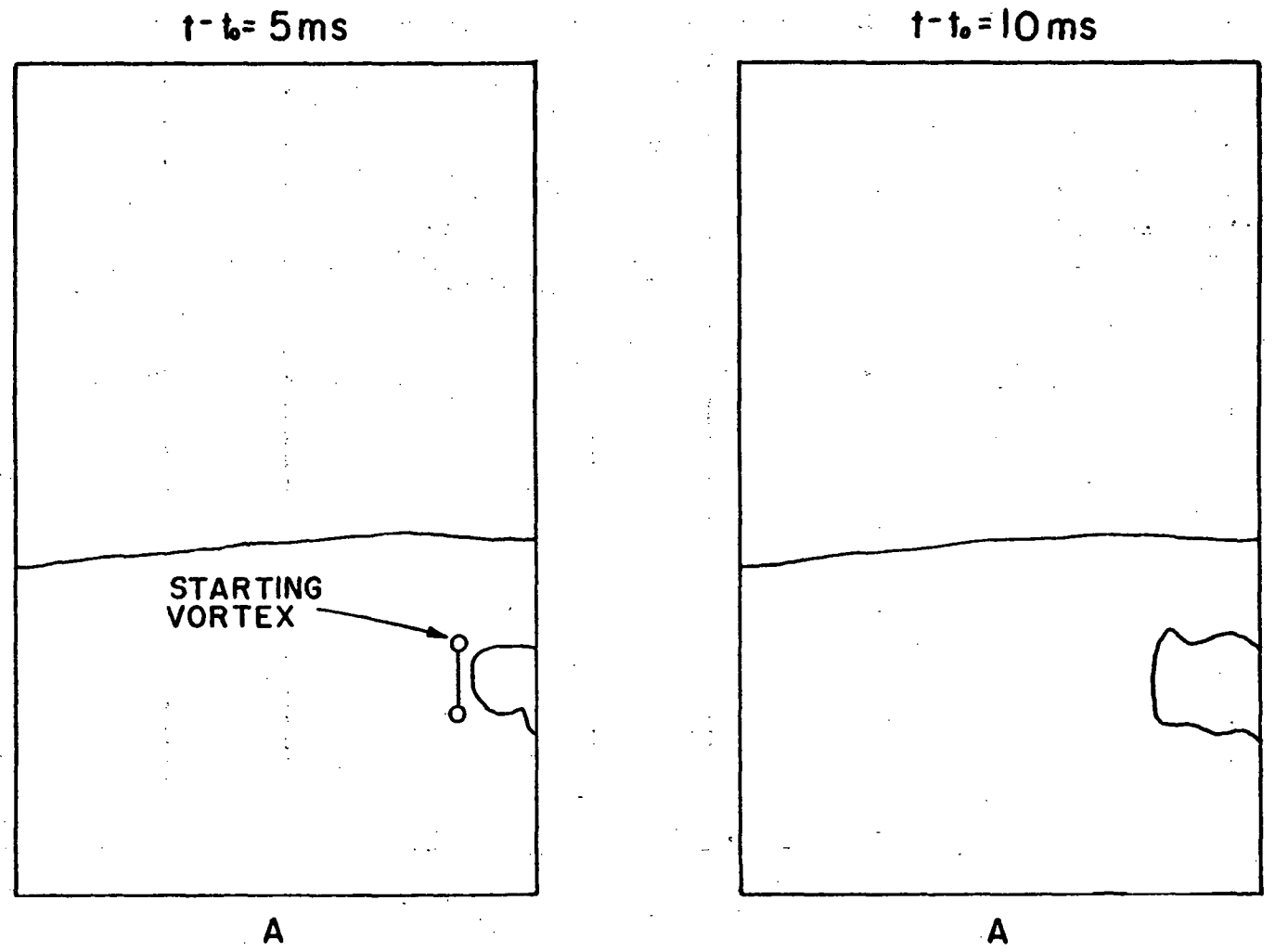

Figure 16: Case 3 at $t-t_o$ = 5 ms, $t-t_o$ = 10 ms.

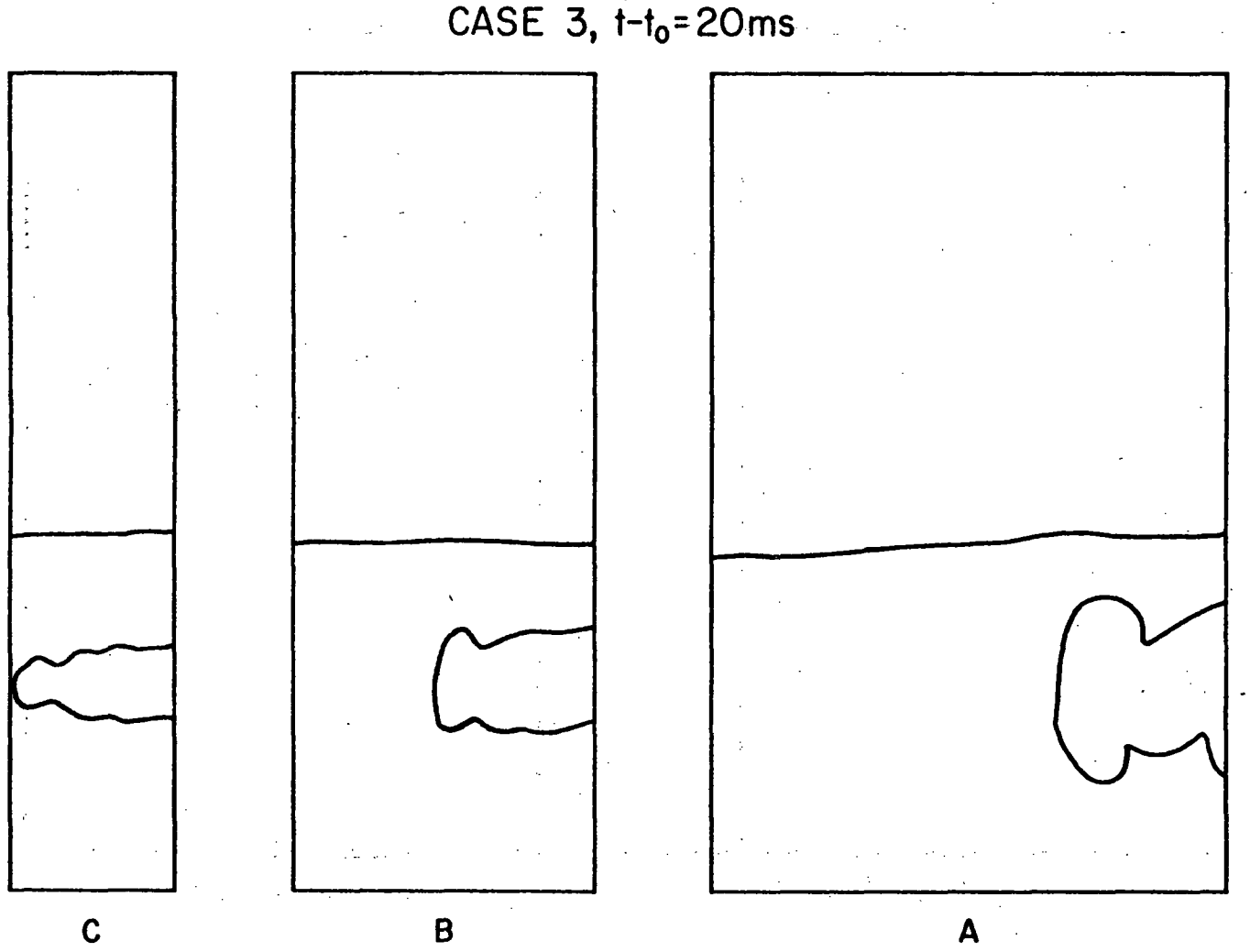

Figure 17: Case 3 at $t-t_0$ = 20 ms.

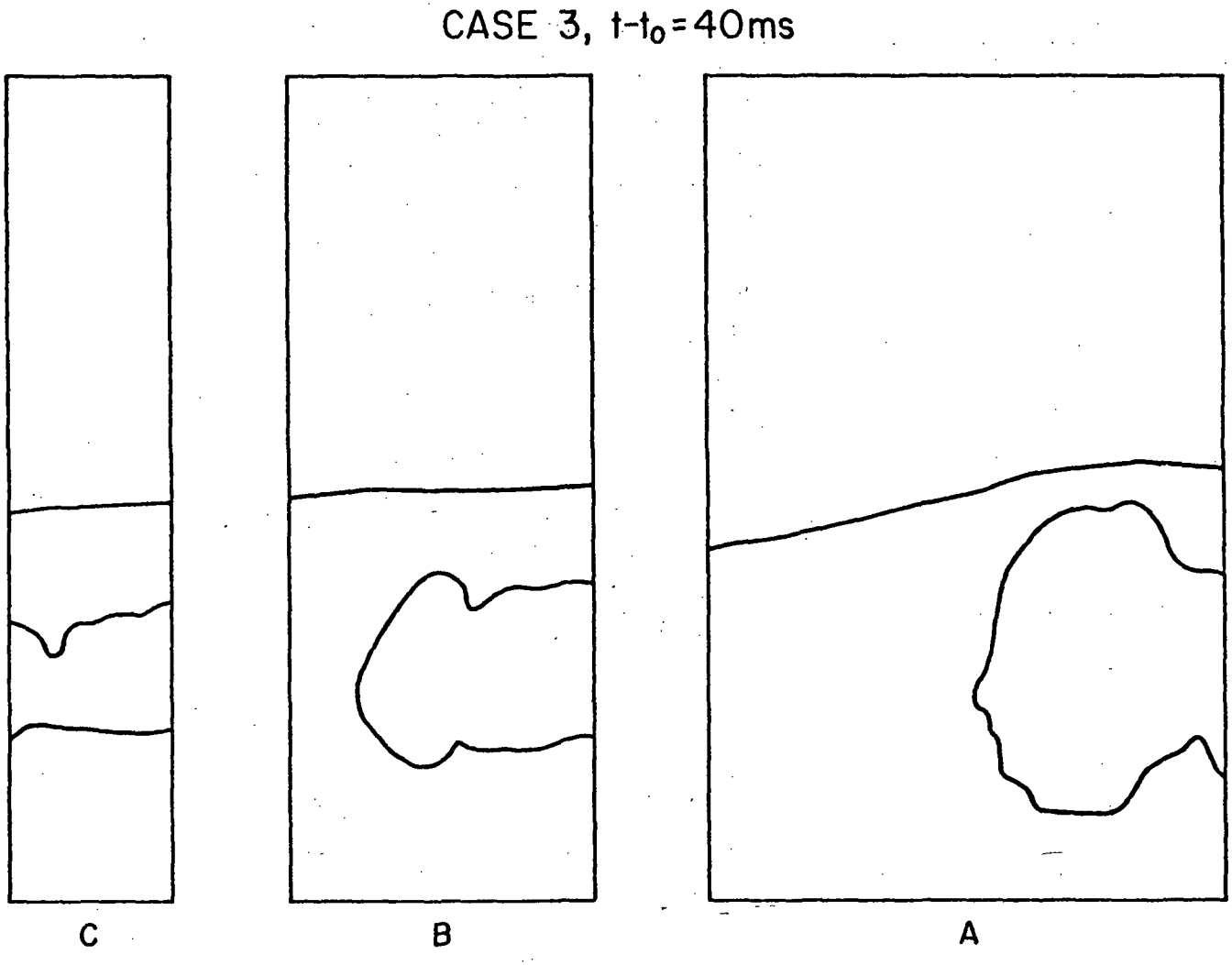

Figure 18: Case 3 at $t-t_o$ = 40 ms.

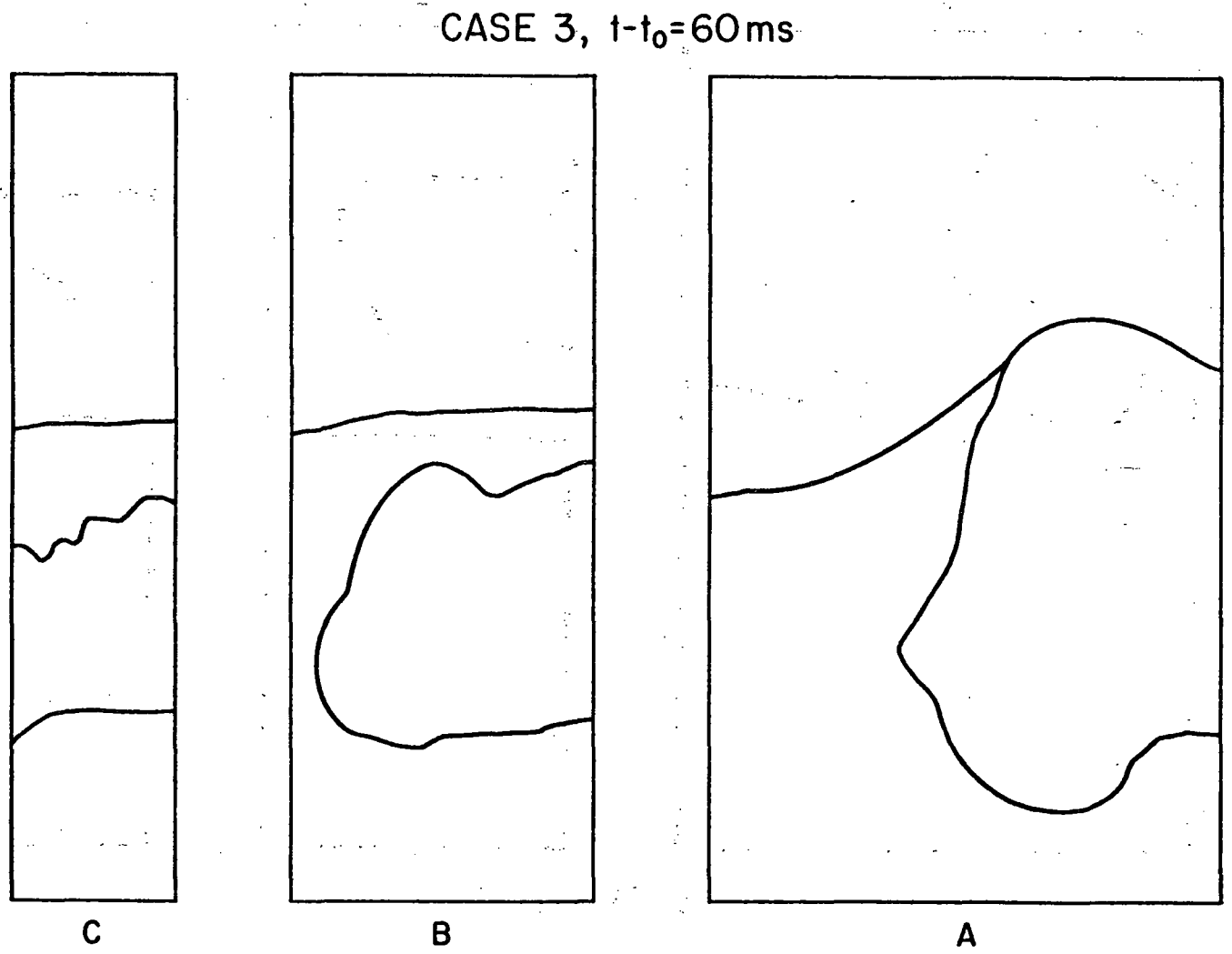

Figure 19: Case 3 at $t-t_o$ = 60 ms.

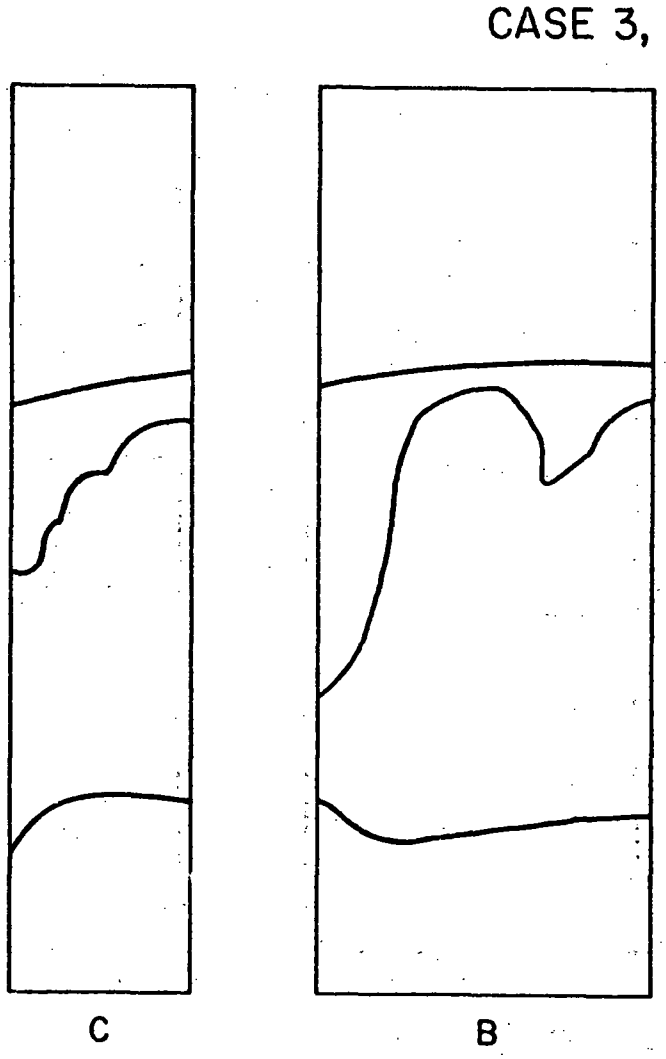

POOL BREAKTHROUGH HAS OCCURRED IN SYSTEM A.

Figure 20: Case 3 at $t-t_o$ = 80 ms.

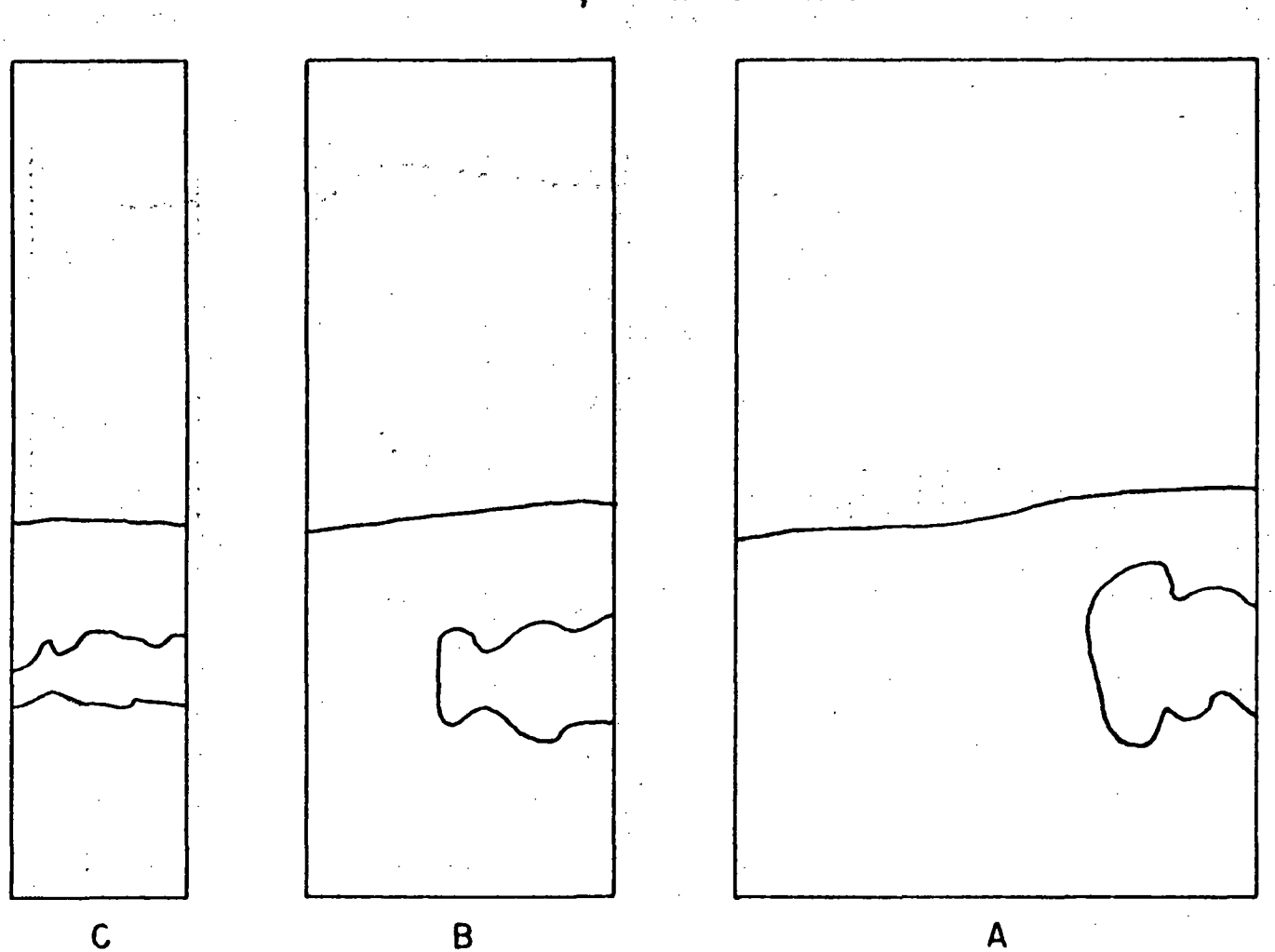

Figure 21: Case 4 at $t-t_0$ = 20 ms.

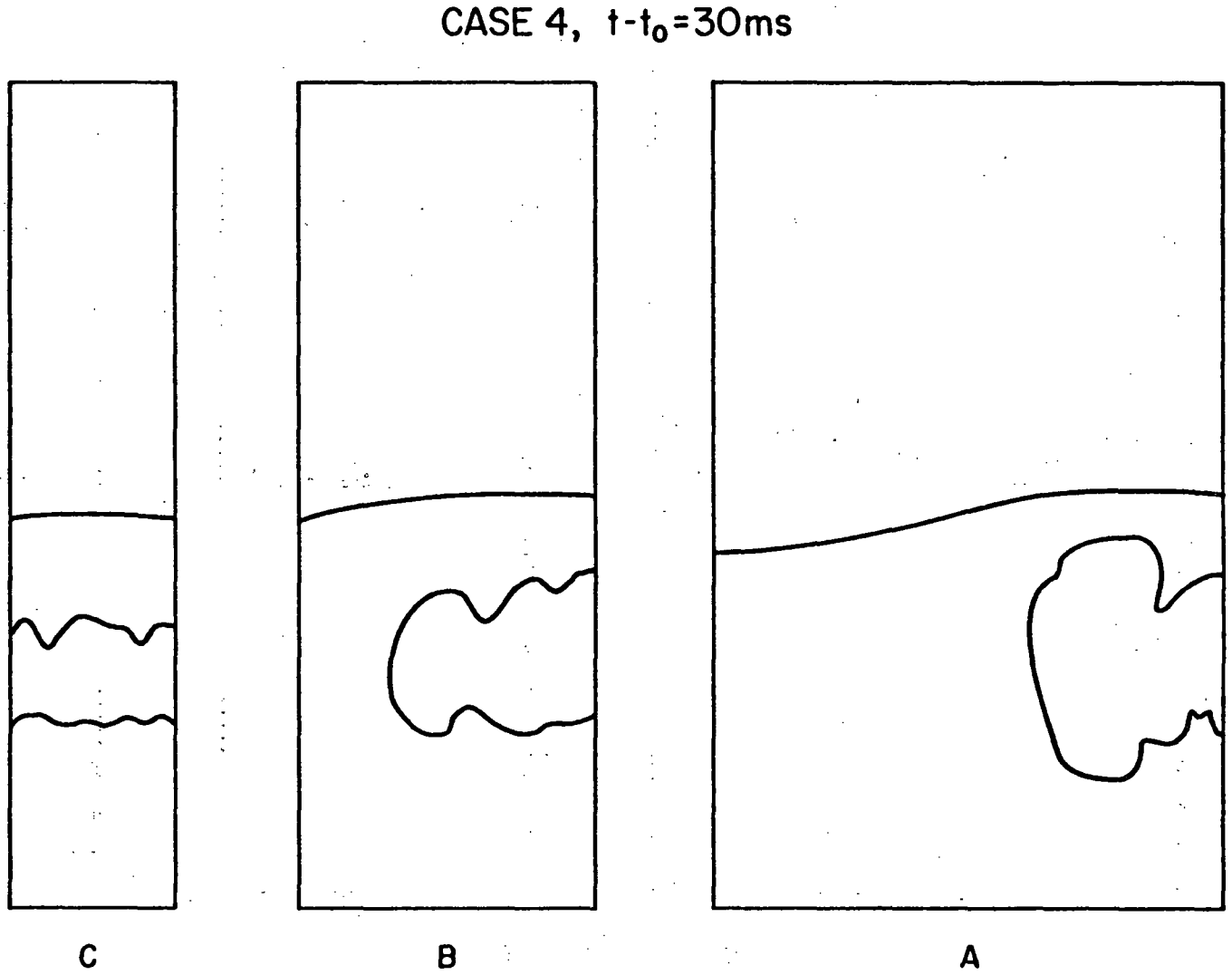

Figure 22: Case 4 at $t-t_o$ = 30 ms.

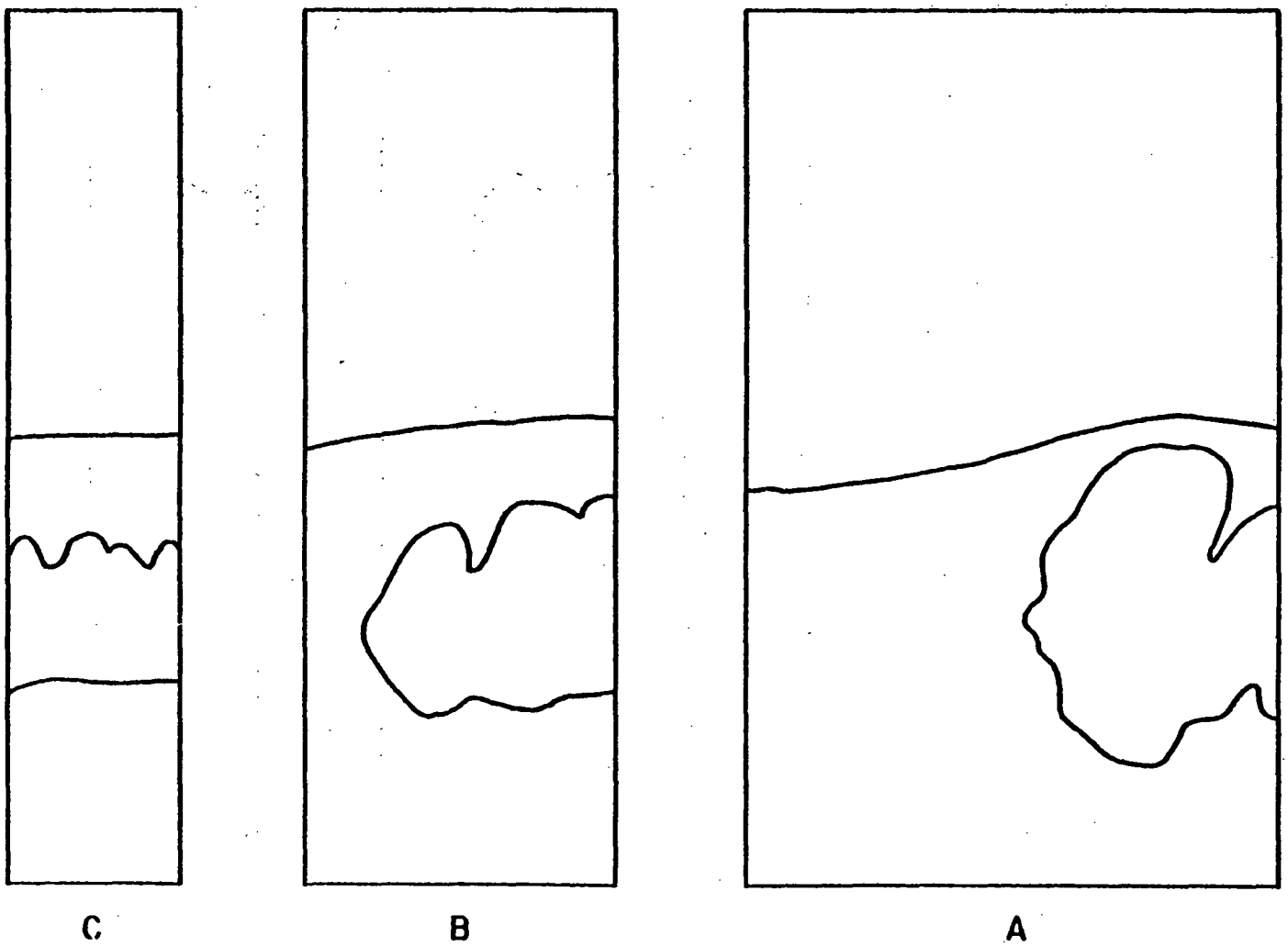

Figure 23: Case 4 at t-t$_0$ = 40 ms.

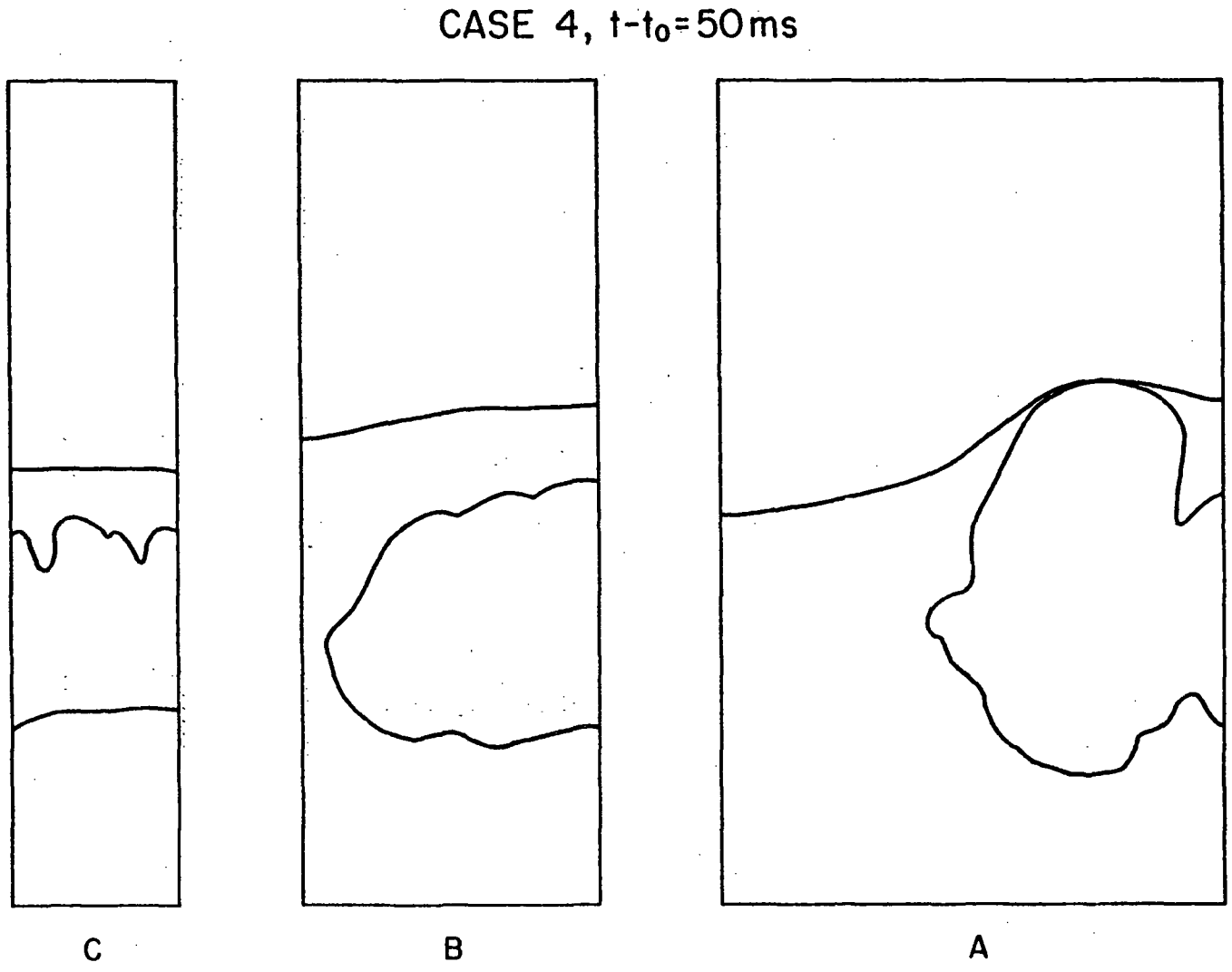

Figure 24: Case 4 at $t-t_o$ = 50 ms.

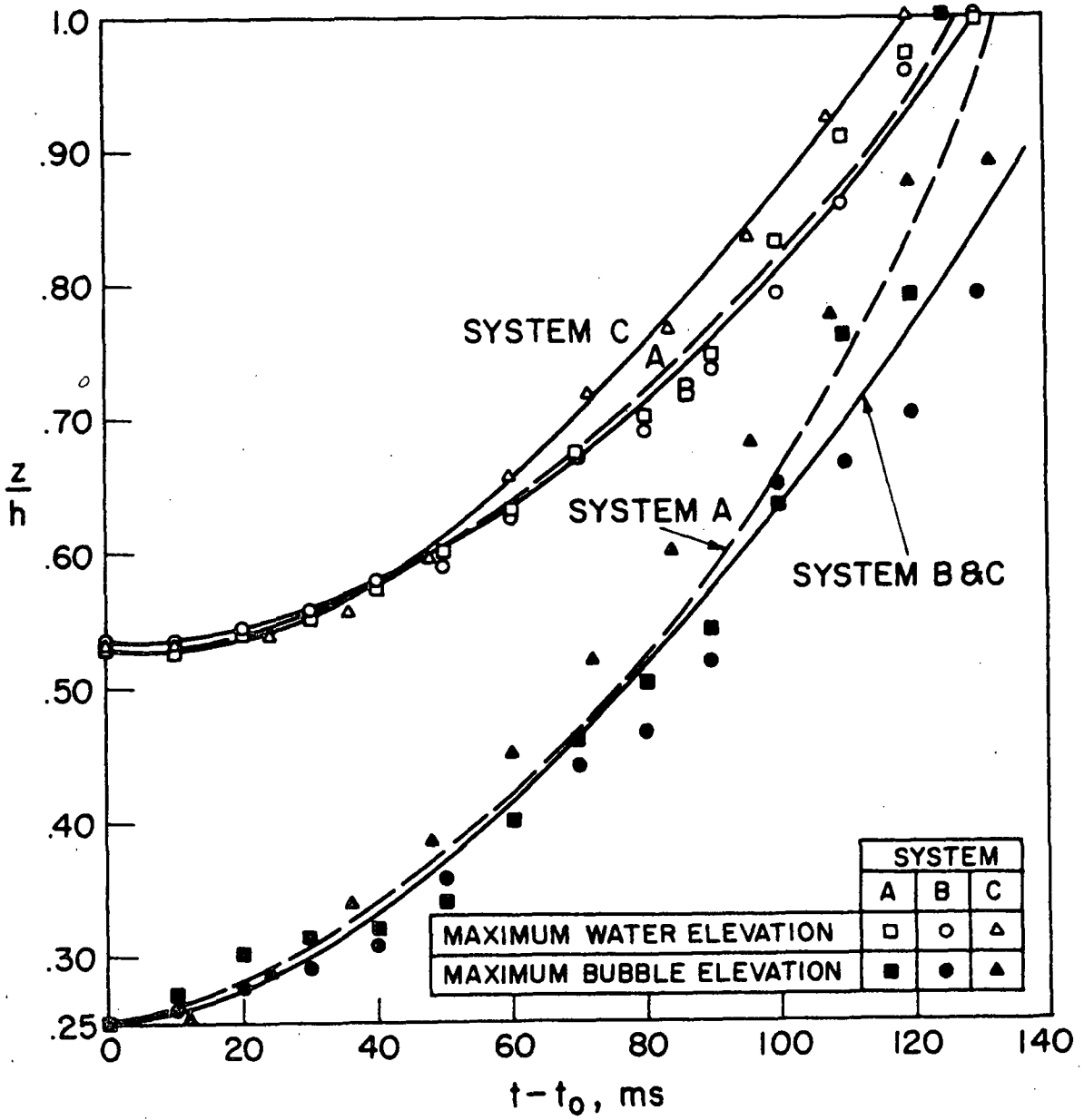

Figure 25: Case 1, water elevations vs time.

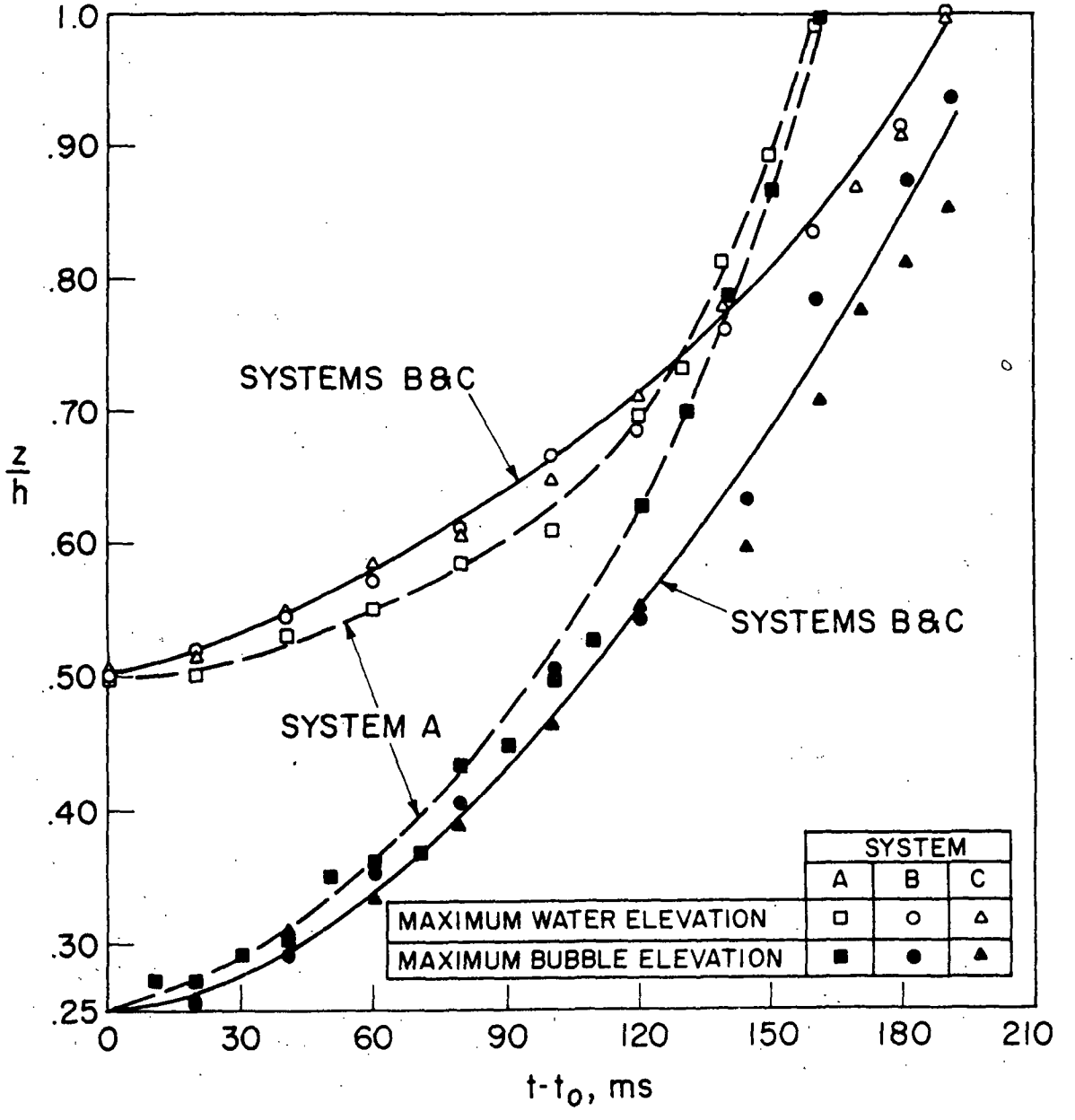

Figure 26: Case 2, water elevations vs time.

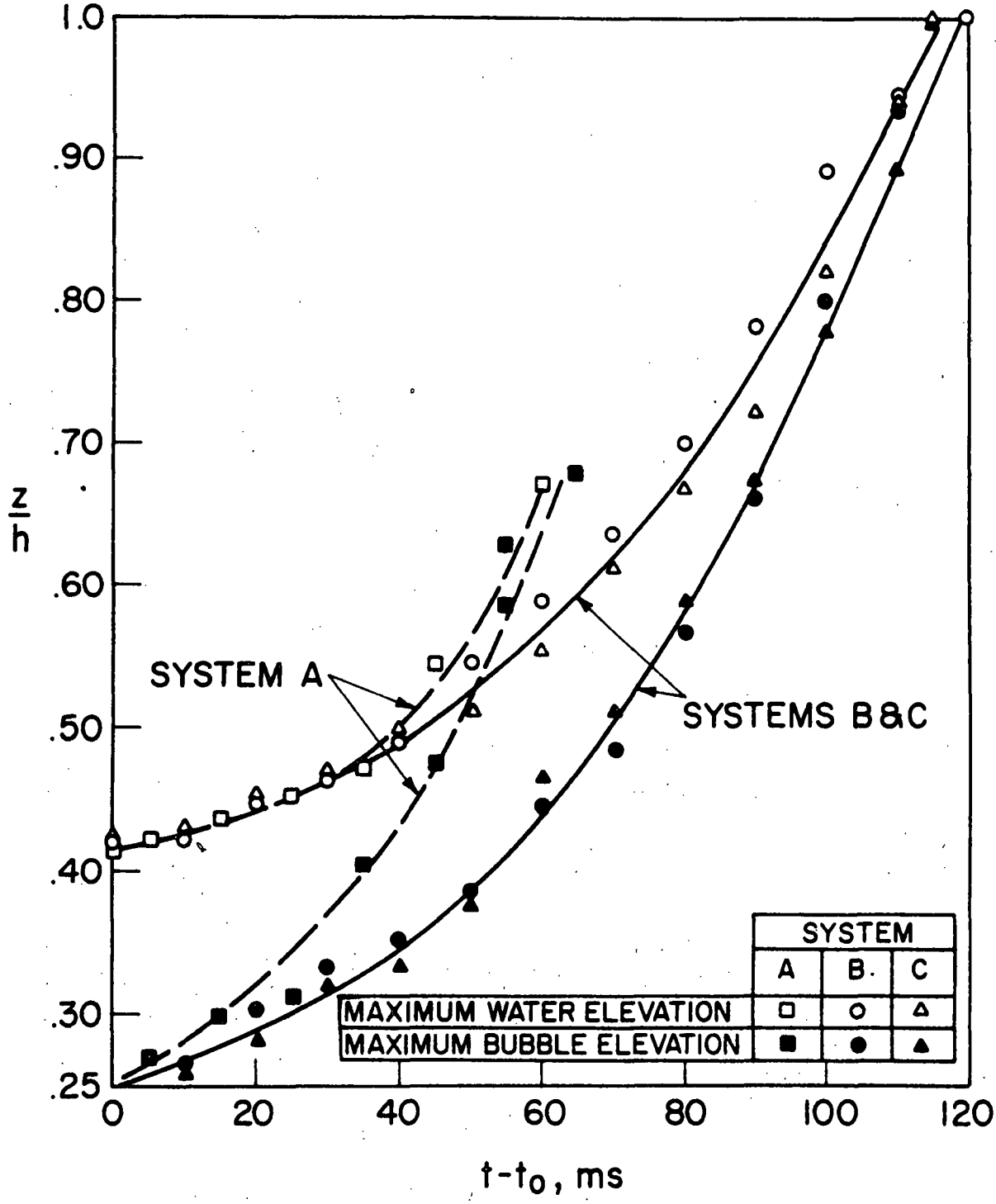

Figure 27: Case 3, water elevations vs time.

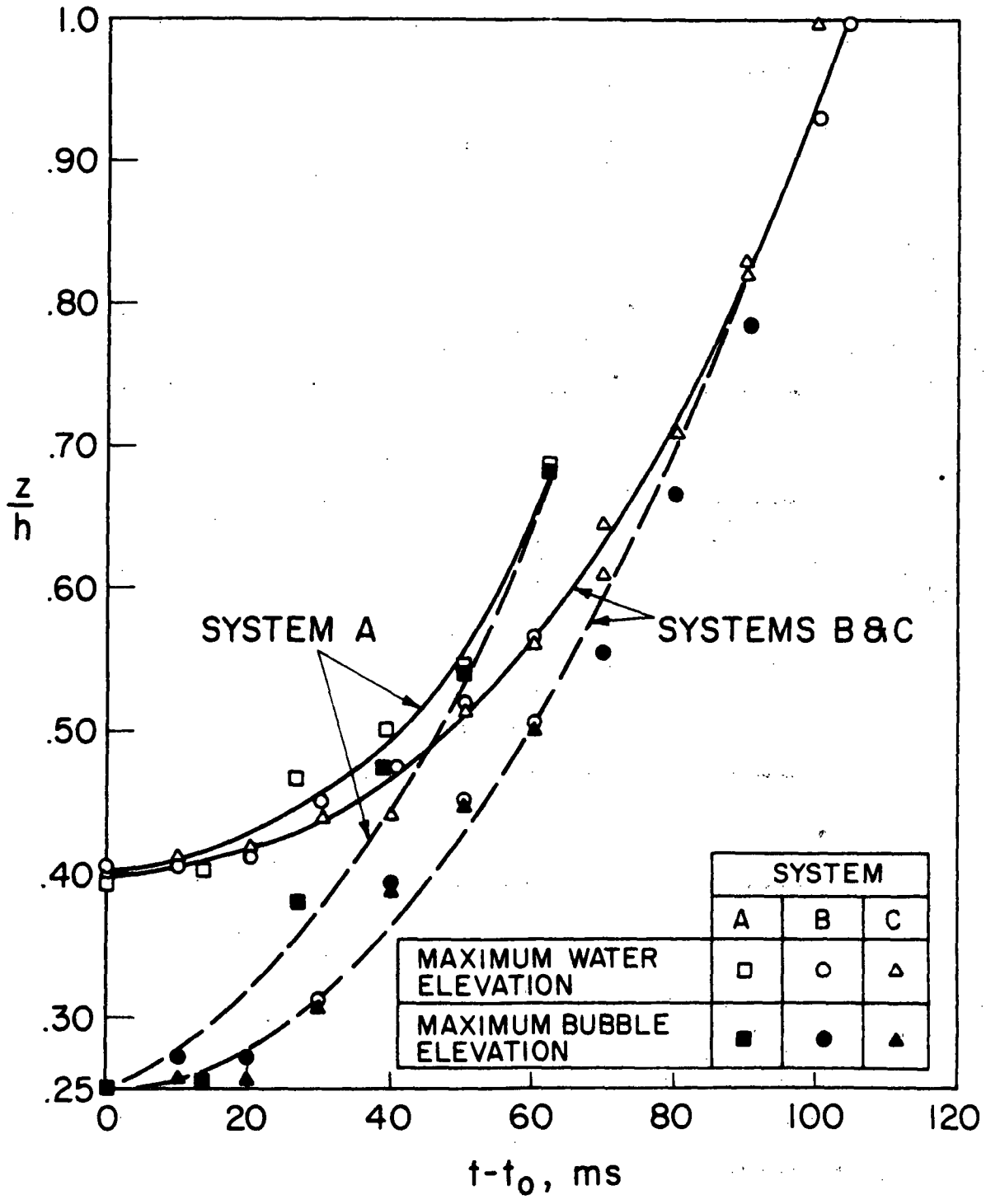

Figure 28: Case 4, water elevations vs time.

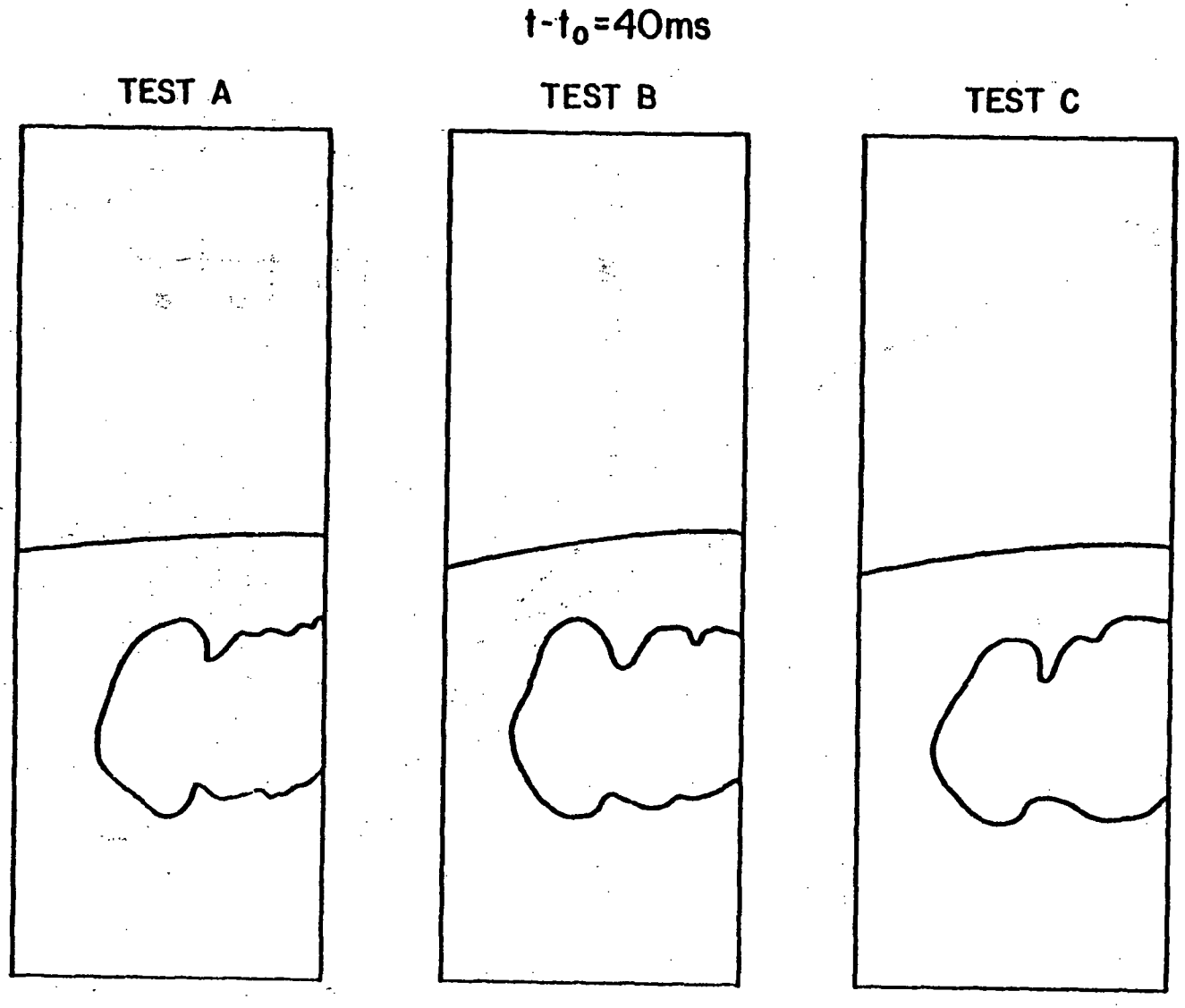

Figure 29: Comparison of three different tests of Case 3 in system B, at $t-t_o$ = 40 ms.

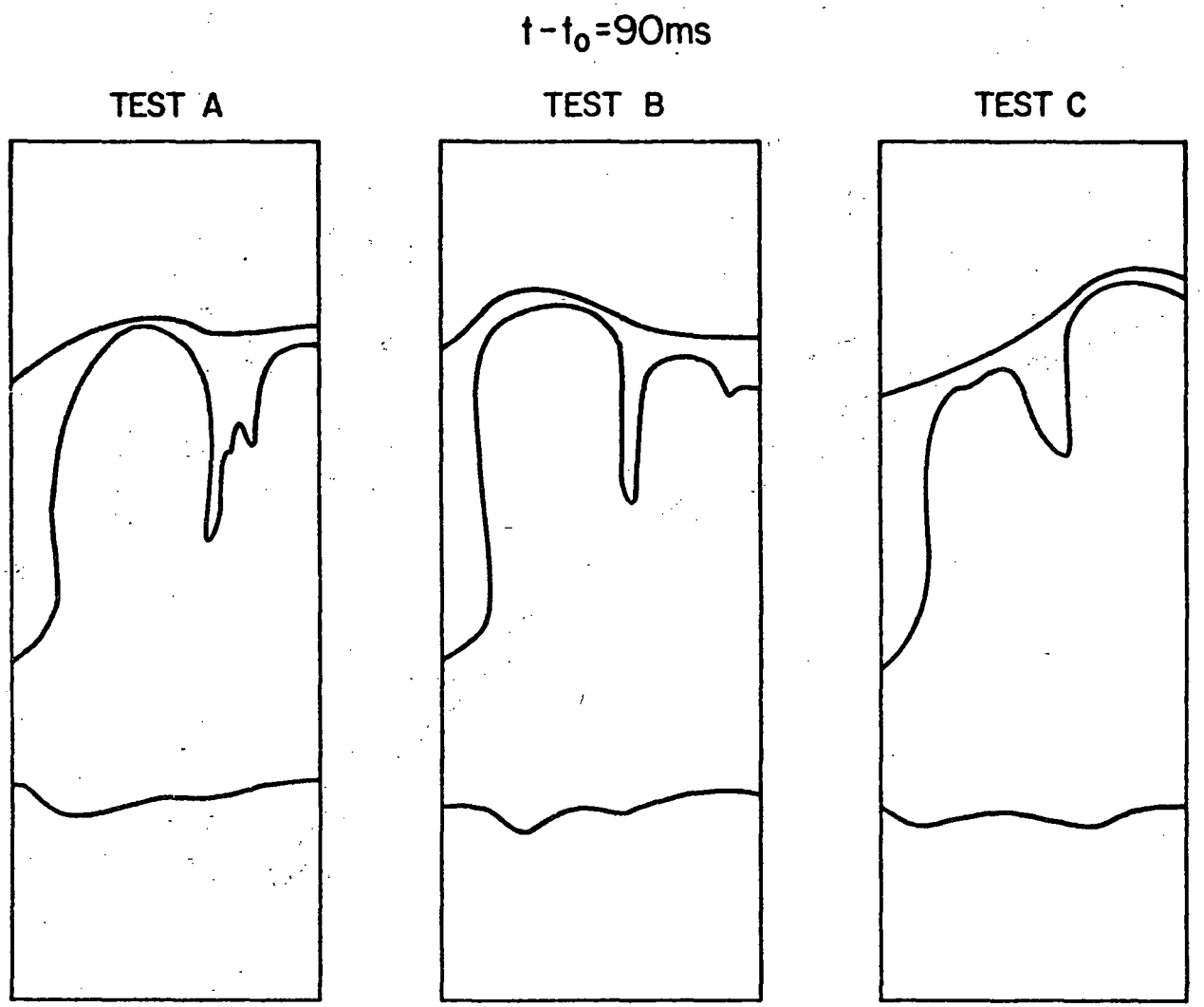

Figure 30: Comparison of three different tests of Case 3 in system B, at $t-t_o$ = 90 ms.

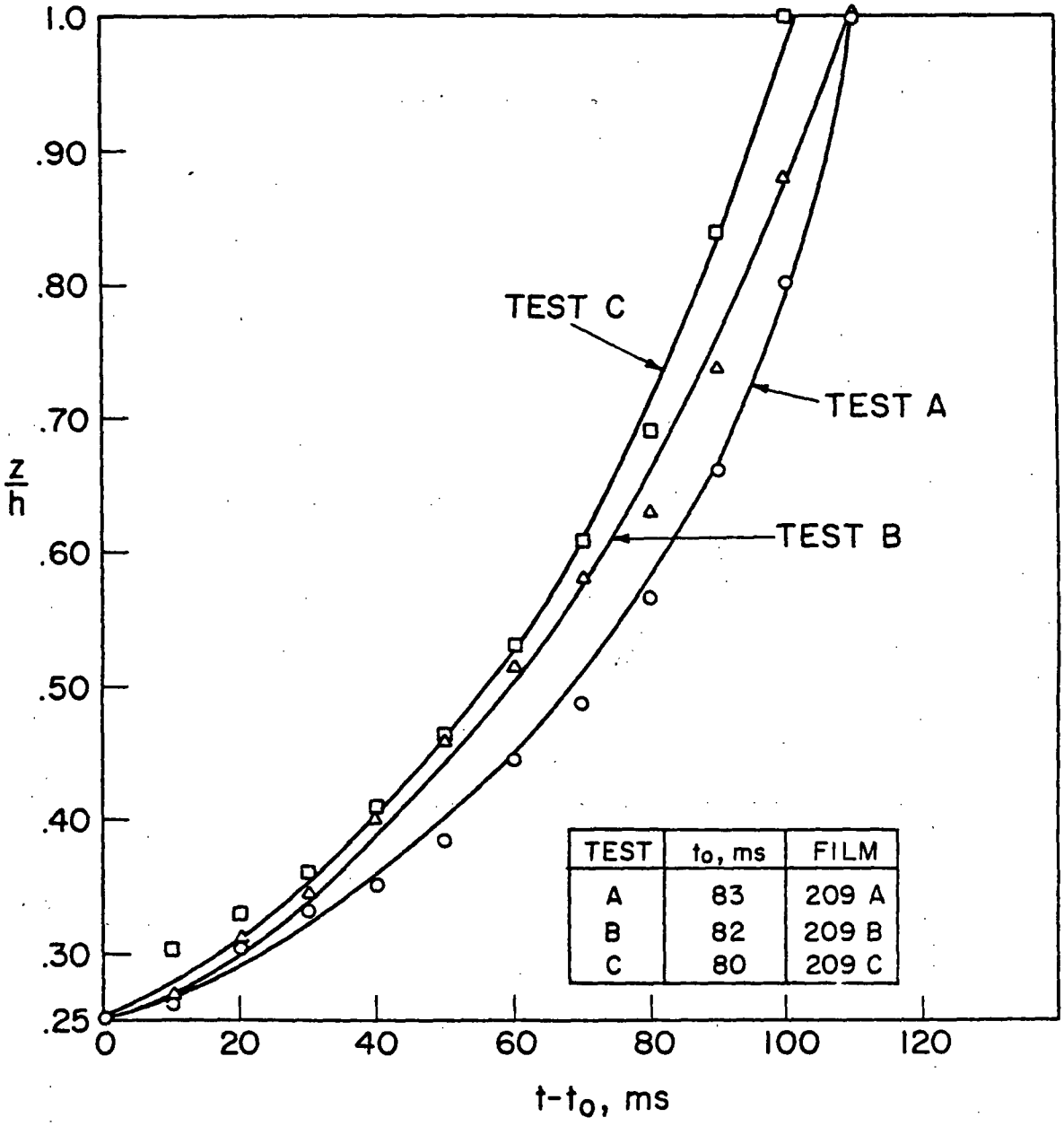

Figure 31: Comparison of water elevations vs. time in the three different tests of Case 3, system B, referred to in Figs. 29 and 39.

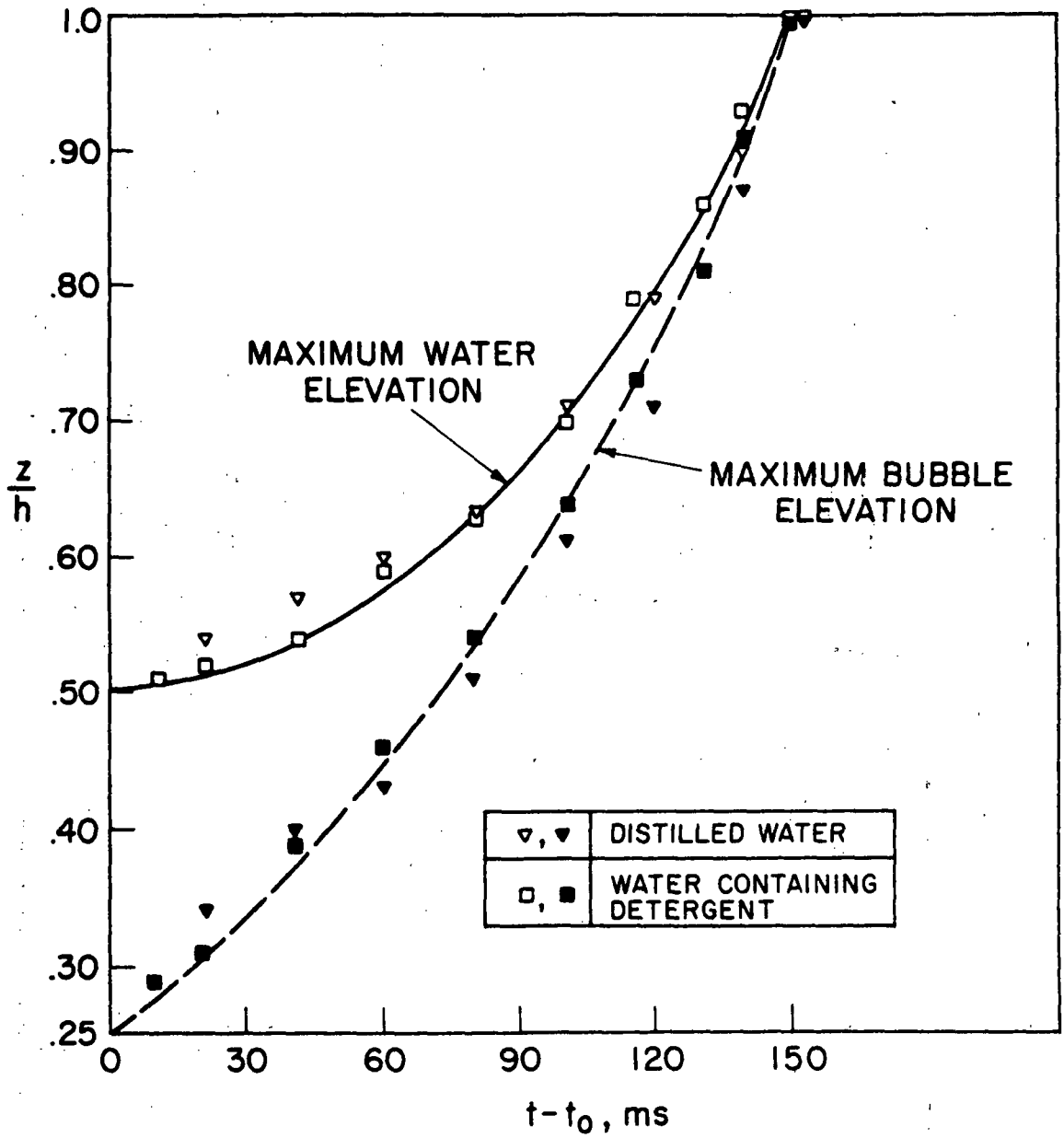

Figure 32: Comparison of two tests in system A, one with distilled water and the other with water containing surfactant. $C_m = 0.20$, $s/\ell_v = 1.67$, $c_m(RT_D/g\ell v)^{1/2} = 62$, $p_D/p_w = 2.0$.

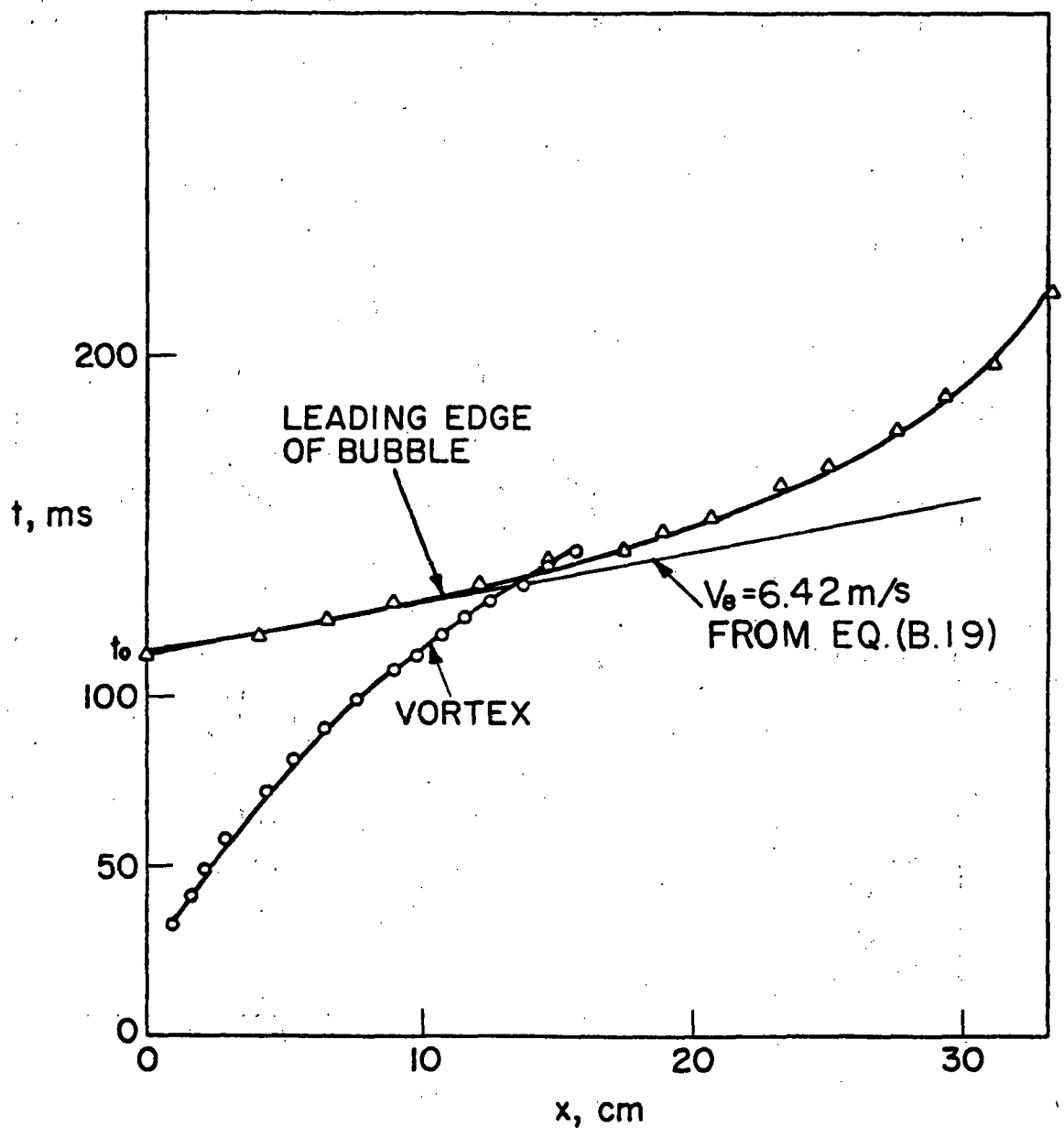

Figure 33: Case 1, Horizontal displacements of starting vortex and bubble leading edge vs time in system A.

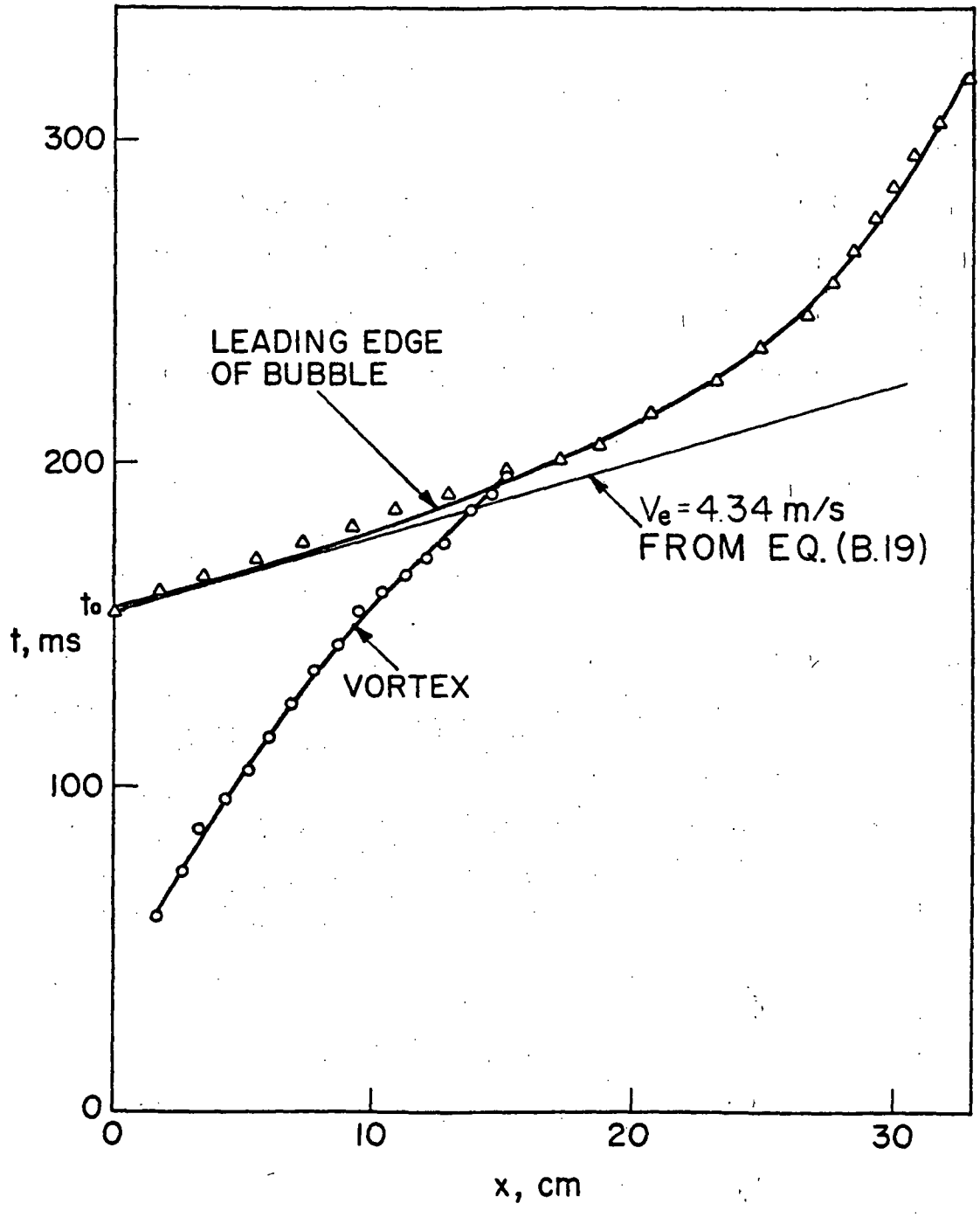

Figure 34: Case 2, Horizontal displacements of starting vortex and bubble leading edge vs time in system A.

APPENDIX A: RELATIONSHIP BETWEEN POOL PRESSURE OSCILLATIONS AND WALL ACCELERATIONS.

What follows is an approximate model which links the pool pressure oscillations with the side wall accelerations. The basic assumption is that the side wall oscillation is the driving force for the pool oscillation which in turn induces a pressure oscillation at other points in the pool. The purpose of this model is to show that the observed pool pressure oscillations were roughly consistent with the observed side wall accelerations.

Let the outward displacement of the side wall at y, z (see Fig. A.1) be

$$x(y,z,t) = x_o \sin \frac{\pi z}{h} \sin \frac{\pi y}{b} \sin \frac{2\pi t}{\tau} \qquad (A.1)$$

where τ is the period of the wall oscillation, x_o is its amplitude at the center of the side wall, t is time, and the other quantities are defined in Fig. A.1.

The upward pool velocity v at z due to wall oscillation is obtained in terms of x (y,z,t) from the mass conservation equation,

$$\rho v b w = - \frac{d}{dt} \left[\rho b w z + 2\rho \int_o^z \int_o^b x \, dy \, dz \right] \qquad (A.2)$$

Here, ρ is the fluid density. Using Eq. (A.1) in Eq. (A.2), we obtain

$$v = - \frac{8}{\pi} \frac{x_o h}{w\tau} \left[1 - \cos \frac{\pi z}{h} \right] \cos \frac{2\pi t}{\tau} \qquad (A.3)$$

The vertical pressure gradient in the fluid is given by the equation of motion (with the convective acceleration term neglected, for obvious reasons):

$$\frac{\partial p}{\partial z} = - \rho \frac{\partial v}{\partial t} \quad . \tag{A.4}$$

Substituting Eq. (A.3) into the right-hand side of Eq. (A.4) and integrating from z to z_w, we obtain the pressure in the fluid at elevation z as

$$p(z, t) = p_w + \frac{16\rho x_o h}{w\tau^2} \sin \frac{2\pi t}{\tau} \left[(z_w - z) - \frac{h}{\pi} \cdot (\sin \frac{\pi z_w}{h} - \sin \frac{\pi z}{h})\right] \tag{A.5}$$

where p_w is the pressure in the wetwell airspace, and z_w is the elevation of the top water surface in the pool. Now if an accelerometer is placed on the side wall at $y = \frac{b}{2}$ and at an elevation $z = z_a$, then the acceleration read by it is obtained from Eq. (A.1) as

$$a = \ddot{x} \ (z = z_a, \ y = b/2)$$

$$= - \frac{4\pi^2 x_o}{\tau^2} \sin \frac{2\pi t}{\tau} \sin \frac{\pi z_a}{h} \tag{A.6}$$

Eq. (A.6) can be substituted into Eq. (A.5) to eliminate x_o. We then obtain the following relation for the pressure at z:

$$p(z, t) = p_w - \Delta p \sin \frac{2\pi t}{\tau} \tag{A.7}$$

where

$$\Delta p = \frac{4}{\pi^2} \frac{\rho h a}{w} \left[\frac{(z_w - z) - \frac{h}{\pi} \left(\sin \frac{\pi z_w}{h} - \sin \frac{\pi z}{h} \right)}{\sin \frac{\pi z_a}{h}} \right] \qquad (A.8)$$

Consider now the data shown in Fig. 5a. Both the pressure trace and the accelerometer trace show components at a common period of the order of 6 ms (the accelerometer also shows a higher frequency component). Just after the initiation of the blowdown, for example, the accelerometer shows peak accelerations of about $(\frac{1}{3})g$ at this frequency. Now for the case under consideration (System B, case 1), h = 0.6 m, w = 0.075 m and $z_w^* = 0.30$ m. The pressure gauge was mounted at z = 0 m and the accelerometer at $z_a = 0.30$ m. Eq. (A.8) then predicts

$$\Delta p = 1.2 \text{ kPa}$$

for $a \approx (\frac{1}{3})$ g. This compares favorably with the observed pressure oscillation amplitude, which is about 1.5 kPa.

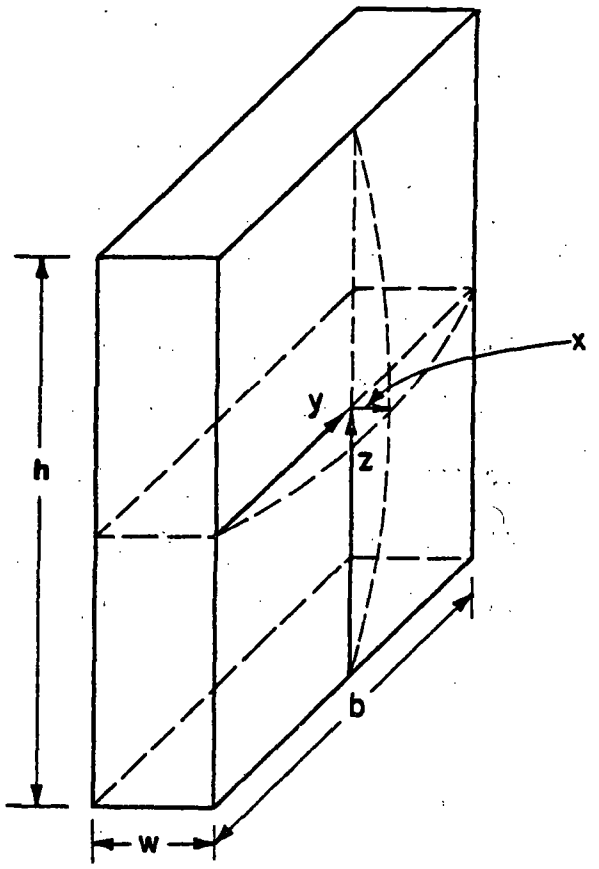

Figure A.1: Notation for Appendix A.

APPENDIX B: QUANTITATIVE ANALYSIS OF VENT CLEARING PROCESS.

The vent clearing process consists of two parts. First, the water is cleared from the vertical pipe, and then the water slug is cleared from the horizontal vent itself. We shall develop a simple model for these processes by assuming one-dimensional flow and that the pressure on the upstream water interface is constant at the dry-well pressure p_D.

First, consider the clearing from the vertical pipe. Applying the unsteady Bernoulli equation along a streamline from the upstream water interface to the vent exit, (where the pressure is $p_w + \rho g s$) and accounting for the inertia of the water jet at the vent exit by adding a length of one pipe diameter to the integration path, (Fig. B.1), we get the equation

$$\rho \left(x \frac{A_v}{A_p} + \ell_v + d \right) \frac{dV_v}{dt} + \left(1 + k - \frac{A_v^2}{A_p^2} \right) \frac{1}{2} \rho V_v^2 = p_D - p_w - \rho g (s-x) \qquad (B.1)$$

Here, V_v is the velocity in the vent pipe, x is the elevation of water in the vertical pipe (Fig. B.1), and we have assumed that the fricitional losses are $\frac{1}{2} \rho k V_v^2$ and have used the mass conservation equation

$$A_v V_v = A_p V_p \qquad (B.2)$$

where

$$V_p = -\frac{dx}{dt} \tag{B.3}$$

is the downward velocity in the vertical pipe.

Eqs. (B.1) - (B.3) can in principle be solved numerically, with the initial conditions $x = 0$ and $V_v = 0$ at $t = 0$. A simple analytic solution is available when one makes the assumptions, quite reasonable in our case, that

$$\frac{xA_v}{A_p} << \ell_v + d \tag{B.4}$$

$$\rho g\,(s - x) << p_D - p_w \tag{B.5}$$

Eq. (B.1) than takes the form

$$\rho\,(\ell_v + d)\,\frac{dV_v}{dt} + \left[1 + k - \frac{A_v^2}{A_p^2}\right]\frac{1}{2}\,\rho V_v^2 = p_D - p_w \tag{B.6}$$

and has the straightforward solution

$$V_v = V_o\,\frac{1 - e^{\frac{-t}{\tau}}}{1 + e^{\frac{-t}{\tau}}} \tag{B.7}$$

where

$$V_o = \left[\frac{2(p_D - p_w)}{\rho\left(1 + k - \frac{A_v^2}{A_p^2}\right)}\right]^{1/2} \tag{B.8}$$

$$\tau = \frac{1}{1 + k - \frac{A_v^2}{A_p^2}} \left(\frac{\ell_v + d}{V_o} \right) \tag{B.9}$$

This solution is sketched in Fig. B.2. It is valid up to the time t* where the air reaches the upstream end of the vent pipe. That time is determined from the mass conservation relation.

$$A_v \int_0^{t^*} V_v \, dt = A_p s \tag{B.10}$$

After the air enters the horizontal vent, the governing equation changes. Bernoulli's equation, applied from the upstream edge of the water slug to the exit, allowing an extra diameter length for the inertia of the jet, now yields

$$\rho \, (x' + d) \, \frac{dV_v}{dt} = p_D - p_w - \rho g s \tag{B.11}$$

where x' is indicated in Fig. B.1. We have assumed no viscous losses in the vent itself: The viscous losses are associated primarily with the bend at the vent entrance. The variables V_v and x' are related by

$$V_v = - \frac{dx'}{dt} \tag{B.12}$$

Eqs. (B.11) and (B.12) can be combined into the form

$$- \rho \, (x' + d) \, V_v \, \frac{dV_v}{d(x' + d)} = p_D - p_w - \rho g s \tag{B.13}$$

which can be integrated to yield

$$V_v^2 = V_v^2\,(t^*) - \frac{2\left(p_D - p_w - \rho g s\right)}{\rho}\,\ell n\left(\frac{x' + d}{\ell_v + d}\right) \qquad (B.14)$$

where $V_v(t^*)$ is the solution of Eq. (B.7) at the time t^* corresponding to (B.10), when the air first enters the vent. From Eqs. (B.14) and (B.12), with the initial condition $V_v = V_*$ at $t = t^*$, it is possible in principle to obtain $V_v(t)$ for times between t^* and the vent clearing time t_o. The vent clearing time t_o is then obtained from the water volume conservation requirement that

$$A_v \int_o^{t_o} V_v\, dt = A_p s + A_v \ell_v \qquad (B.15)$$

For the purposes of this appendix, we take a much simplified, approximate approach. In our tests, conditions were such that the initial rise time of V_v, as given by Eqs. (B.9) and (B.8), is fairly short compared with t_o, and the difference between t_o and t^* is also fairly short compared with t_o. We therefore make the approximation [see Eq. (B.7)] that

$$V_v \simeq V_o = \left[\frac{2\left(p_D - p_w\right)}{\rho\left(1 + k - \frac{A_v^2}{A_p^2}\right)}\right]^{1/2} \qquad (B.16)$$

during the entire vent clearing process (see Fig. B.2), and hence the

vent clearing time t_o follows from Eq. (B.15) as

$$t_o = \left[\frac{\rho\left(1 + k - \frac{A_v^2}{A_p^2}\right)}{(2\,p_D - p_w)}\right] \ell_v \left(1 + \frac{A_p}{A_v}\,\frac{s}{\ell_v}\right) \qquad (B.17)$$

Table B.1 lists values of t_o computed from Eq. (B.17), compared with the experimentally measured values. The value of k for each of the three systems (k = 0.50 for A, 1.0 for B, and 1.5 for C) was chosen so as to make the comparison as good as possible. The facts that the values of k which fit the data are quite reasonable on physical grounds, and the observed trends are reasonably well predicted, gives some credence to this simple model for clearing.

Another vent clearing parameter which could be determined from the experimental data was the final exit velocity V_e of the slug, equal to our Eq. (B.14) predicts this velocity as

$$V_e = V_v(t^*)\left[1 + \frac{2(p_D - p_w - \rho g s)}{\rho\, V_v^2(t^*)}\;\ell n\left(\frac{\ell_v}{d} + 1\right)\right]^{1/2} \qquad (B.18)$$

If we take $V_v(t^*) \approx V_v$, the latter given by Eq. (B.8), this becomes

$$V_e = \left[\frac{2p_w}{\rho}\,\frac{\left(\frac{p_D}{p_w} - 1\right)}{\left(1 + k - \frac{A_v^2}{A_p^2}\right)}\right]\left[1 + \frac{\left(\frac{p_D}{p_w} - 1 - \frac{\rho g s}{p_w}\right)}{\left(\frac{p_D}{p_w} - 1\right)}\left(1 + k - \frac{A_v^2}{A_p^2}\right)\ell n\left(\frac{\ell_v}{d} + 1\right)\right]$$

The final water exit velocity predicted by Eq. (B.19) is compared with the observed bubble pool entry velocities in Figs. 33 and 34. The value of k is taken as in Table B.1. The agreement is remarkably good.

TABLE B.1: VENT CLEARING TIMES t_o PREDICTED FROM EQ. (B.17).

Comparison No.	System A, with k=0.50	System B, with k=1.00	System C, with k=1.50
1	103 ms	121 ms	136 ms
2	145	170	193
3	70	83	93
4	70	83	93

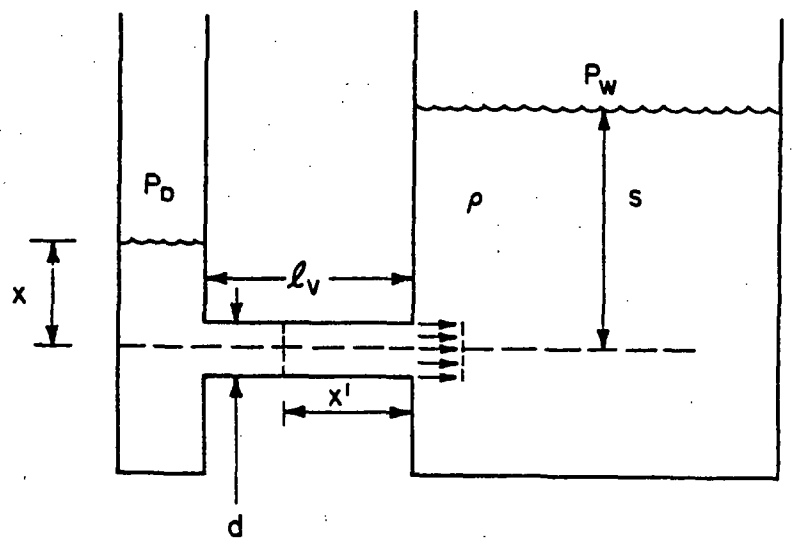

Figure B.1: Notation for Appendix B.

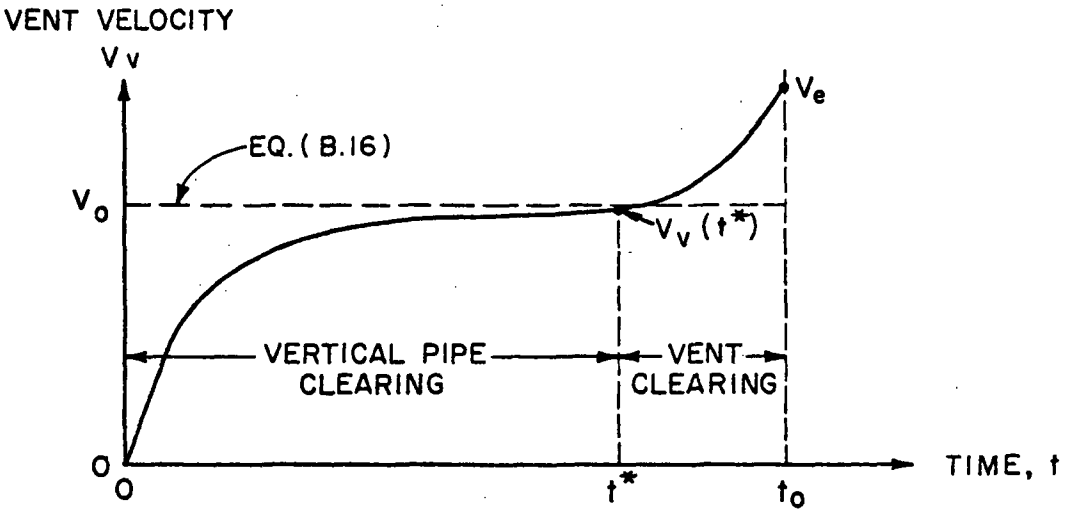

Figure B.2: Sketch of vent velocity, and value predicted by Eq. B.16.

*U.S. GOVERNMENT PRINTING OFFICE: 1980 620-269/125 1-3

NRC FORM 335 (7-77) U.S. NUCLEAR REGULATORY COMMISSION

BIBLIOGRAPHIC DATA SHEET

1. REPORT NUMBER *(Assigned by DDC)*
NUREG/CR-1444

4. TITLE AND SUBTITLE *(Add Volume No., if appropriate)*
Investigation of Distorted-Geometry Simulation of Pool Dynamics in Horizontal-Vent BWR Containments

2. *(Leave blank)*

3. RECIPIENT'S ACCESSION NO.

7. AUTHOR(S)
N. G. Ruggieri and A. A. Sonin

5. DATE REPORT COMPLETED
MONTH May YEAR 1979

9. PERFORMING ORGANIZATION NAME AND MAILING ADDRESS *(Include Zip Code)*
Massachusetts Institute of Technology
Department of Mechanical Engineering
Cambridge, Mass 02139

DATE REPORT ISSUED
MONTH April YEAR 1980

6. *(Leave blank)*

8. *(Leave blank)*

12. SPONSORING ORGANIZATION NAME AND MAILING ADDRESS *(Include Zip Code)*
Analysis Development Branch
Division of Reactor Safety Research
Office of Nuclear Regulatory Research
Washington, D. C. 20555

10. PROJECT/TASK/WORK UNIT NO.

11. CONTRACT NO.
FIN No. B6167

13. TYPE OF REPORT
Topical Report

PERIOD COVERED *(Inclusive dates)*

15. SUPPLEMENTARY NOTES

14. *(Leave blank)*

16. ABSTRACT *(200 words or less)*

Experiments were conducted to investigate the accuracy of distorted-geometry testing of pool dynamics in horizontal-vent BWR containments. Distorted-geometry testing implies testing in systems where the flow-wise dimensions are full scale, but all dimensions transverse to the flow are reduced in the same proportion. The assumption is that flow velocities, pressures and other thermodynamic properties can be interpreted as being the same in the distorted-geometry system as in its correctly proportioned counterpart. Our experiments, which were done at small scale using the established scaling laws, showed that the geometric distortions can have a significant effect on the pool swell under conditions which are roughly representative of horizontal-vent BWR containment systems during a LOCA. Breakthrough occurred later, the water ligament was thicker, and pool velocity lower in a system where the cross-sectional areas were reduced by a factor of three. Some reasons for the differences are discussed.

17. KEY WORDS AND DOCUMENT ANALYSIS

17a. DESCRIPTORS

17b. IDENTIFIERS/OPEN-ENDED TERMS

18. AVAILABILITY STATEMENT

19. SECURITY CLASS *(This report)*

21. NO. OF PAGES

20. SECURITY CLASS *(This page)*

22. PRICE
$

UNITED STATES
NUCLEAR REGULATORY COMMISSION
WASHINGTON, D. C. 20555

OFFICIAL BUSINESS
PENALTY FOR PRIVATE USE, $300

POSTAGE AND FEES PAID
U.S. NUCLEAR REGULATORY
COMMISSION

120555004118 4 ANR4
US NRC
RES ANALYSIS DEVELOPMENT
BRANCH CHIEF
1130SS
WASHINGTON DC 20555